Journal of Computational Applied Mechanics 2026, 57(2): 296-325

DOI: 10.22059/jcamech.2026.410269.1769

RESEARCH PAPER

Computational Fluid Dynamics Simulation of Rotor Blade Aerodynamics for the Mars Ingenuity Helicopter

Alex Miller [a], Osman Anwar Bég [a], Tasveer Anwar Bég [b], Muhammad Mubashir Bhatti [c,d,*], Sireetorn Kuharat [a], Ali Kadir [a]

[a] *MPESG, Corrosion Lab, 3-08, Aeronautical and Mechanical Engineering Division, University of Salford, M5 4WT, UK*

[b] *Engineering Mechanics Research, Israfil House, Dickenson Rd., Manchester, M13, UK*

[c] *Department of Physics, College of Science, Korea University, 145 Anam-ro, Seongbuk-gu, Seoul 02841, Republic of Korea*

[d] *Material Science Innovation and Modelling (MaSIM) Research Focus Area, North-West University (Mafikeng Campus), Private Bag X2046, Mmabatho 2735, South Africa*

Abstract

The Mars Ingenuity helicopter, a coaxial rotor aerial vehicle, is a pioneering venture into extraterrestrial flight. Rotorcraft technology plays a significant role in future mission development, as it offers advantages for specific applications, particularly in rugged terrain or confined spaces. Mars' landscape presents challenges, including unpredictable wind patterns and dust particles. To fly in the thin, predominantly carbon-dioxide-based atmosphere, rotor blades are designed for efficiency in low density environments with a large blade diameter. This work examines the aerodynamic performance of the blade configuration in a quadcopter Mars Ingenuity design using ANSYS FLUENT computational fluid dynamics. A detailed rotor blade model for CFD analysis has been developed for flow behavior around the rotor blades in Mars atmospheric conditions. Data from the Mars 2020 mission and the Mars Ingenuity Helicopter is used as a baseline. Extensive simulations are described for contour plots and flow vectors, focusing on vortex effects and performance in the Mars atmosphere. The study also addresses unsteady airflow around the rotor disk, leading to instabilities such as blade-vortex interactions and retreating blade stall. Future pathways include control aspects of the blade configuration and blade twist.

Keywords: Mars Ingenuity helicopter; quadcopter blade aerodynamics; vortex flow; ANSYS FLUENT; CFD.

1. Introduction

The overarching goal of the MARS Ingenuity helicopter is to demonstrate the feasibility of aerial mobility on Mars with the aim of producing the equivalent vertical flight capabilities of an Earthbound helicopter in a low-

[*] Corresponding author.
E-mail address: mmbhatti@korea.ac.kr

density atmosphere, where the number one limitation is a reduction in lift capacity. Achieving this goal will eventually bridge the resolution gap between orbiters providing low-resolution images over large areas, and land-based rovers which provide very high-resolution imagery but are limited by line-of-sight visibility, as noted by Grip et al. [1]. The combination of the rover and rotorcraft is advantageous with respect to reconnaissance tasks, the idea being that the rotorcraft has a better vantage point when scouting potential regions of interest for scientific research. Advancements in conceptual designs for future rotorcraft are already in development with aims of the next generation of Martian air vehicles being able to carry payloads for scientific activities such as sample collection and retrieval, with longer flight time. A prominent area of development is the rotor system, specifically evaluating the aerodynamic performance of the rotor blades and the behaviour of the flow. The challenges inherent to rotary-wing flight are multifaceted. Designing a rotor blade that can effectively overcome unwanted aerodynamic phenomena is crucial to achieving stable and controllable flight. The optimisation of shape, size and material composition is an intricate task with the aim of balancing between lift generation, structural integrity, and weight considerations etc; optimisation involves exploration of parameters such as aerofoil profiles, chord length, twist distribution and blade sweep. With Mars Ingenuity as a development platform, engineers are currently working on identifying optimal rotor blade configurations for low density and ultra-low Reynolds number flight, investigating potential solutions through computational methods including Computational Fluid Dynamics (CFD). Numerical simulation in rotary-wing applications has dramatically increased since the advent of UAVs in the 21st century. Commercial software has become very proficient at accommodating complex geometries and vortical flows which characterize rotary wing aerodynamics. Additionally, very sophisticated in-house vortex codes have been developed by a variety of researchers. Imam and Bicker [2] deployed ANSYS FLUENT to simulate the effects of blade twist on a quadrotor rUAV with the objective of identifying the optimum propellor combination for an efficient and robust flight control system by studying the relationship between thrust, power, and rotor speed in hover with a 1 m⁄s wind speed. The impact of aerodynamic effects on the rUAV when flying at higher speeds had manifested as non-linear disturbances on the airframe and rotor resulting in rotor loading and power demand issues. The investigation implemented a Virtual Blade Model (VBM) via which propeller blades were replaced with momentum sources on an Actuator Disk (AD). This allowed for the pressure jump across the AD to change depending on radius and azimuth, removing requirements for individual blade meshes therefore reducing the time taken to construct a mesh. Blade Element Theory (BET) identified the scale of the momentum sources permitting variations in twist, chord, and aerofoil profiles along the span of the blades. The BET was combined with governing equations in Fluent solved for the non-linear aerodynamic interaction between the propellers and airframe. Haoyuan et al. [3] deployed a CFD code to examine a novel design concept involving chordwise curved wings for a flapping wing rotor (FWR), a relatively new micro aerial vehicle (MAV) which incorporates flapping, rotation and pitching wing motion during both upstroke and downstroke phases of flight. The initial design adopted a flat skeleton attached to a film forming the wing planform, the objective is to advance the aerodynamic performance of the FWR without adding weight by introducing camber. The study included simulations on a three-wing FWR by employing the Reynolds-Averaged Navier-Stokes (RANS) with SST k-omega turbulence model focusing on evaluating the impact of maximum camber and camber position on lift characteristics without changing the projected area, shape, or motion parameters of the wing. Results show a close relationship between wing pressure, flow field and motion period variations, with smaller motion periods over time exhibiting sinusoidal wave-like patterns. Wings with appropriate camber profiles were shown to demonstrate increased lift during flapping attributed to the delayed airflow separation and early attachment of the leading-edge vortex (LEV) to the wing surface. A steady lift increase was observed with camber augmentation up to a maximum camber position of 0.25c where the maximum lift reaches 40% higher than the base (flat) wing design. The simulation conducted a series of ten steps of varying hover altitude with increasing rotor speed between 1000 rpm-14000 rpm. Blade twist of 15°, 25° and 30° for a propellor diameter of 250 mm was simulated for comparison. Results determined that each increase in blade twist saw higher power generation, with a blade twist of 25° producing the highest thrust. Pandey et al. [4] reported on Ansys Fluent CFD simulations of an isolated helicopter rotor in hover for 400 rpm, 600 rpm and 800 rpm at an angle of attack of 8° and based on collective pitch. The 3-bladed rotor was selected from the Eurocopter AS350B3 design with a standard ONERA OA209 aerofoil profile. The rotor blades were meshed using edge and face meshing to account for skewness. The computational domain, based on a closed-test section of a wind tunnel, used both tetrahedral and hexahedral elements. Boundary conditions were set using velocity inlet at 3 m⁄s, and the pressure outlet at normal atmospheric conditions, with the remainder of the domain plus blades set as walls. The k-epsilon turbulence model was selected plus a Moving Reference Frame (MRF), which is a steady-state method specifically applied to simulations involving rotating parts, was utilised to simulate flow over the rotor blades. It was observed that vorticity increases with increasing rotor speed and the strength of the vortices shed from the blade also increases- this results in larger disturbances in the surrounding flow with the curls becoming more tightly packed and organised. For a stable hover a rotor speed of 400 rpm provided the most desirable conditions, which is consistent with values for typical helicopter hover manoeuvres with rotor speeds of 300 rpm- 500 rpm depending on design parameters. Corfield et al. [5] deployed the NASA OVERFLOW-D code, a scalable RANS solver using overset structured grids (a modification of the original NASA OVERFLOW code for moving body and hovering applications) to simulate turbulent aerodynamics for a prototype rotorcraft for use on Mars. They benchmarked the simulations with ongoing hover tests for investigation into rotary-wing technologies on Mars conducted at NASA Ames Research Centre, with the aim of comparing simulated results with results from experimental testing, as noted in Young et al. [6]. The experimental testing was conducted in an environmental chamber where atmospheric conditions replicated the mean surface atmospheric pressure therefore allowing the test to match the operating Reynolds number and Mach number on Mars. The chosen aerofoil for the four-bladed rotor system was an Eppler 387 which is known as a typical low Reynolds number profile section. Test conditions had a Mach tip number of 0.65 and Reynolds number of 50000 based on tip speed and rotor blade chord. The solver was used in conjunction with the OVERGRID package to generate grid systems. The problem domain was split into near-body and off-body grids and the flow solver interpolated the boundary data between each mesh. The near-body grid grids for the single rotor blade contained 1888282 grid points while the off-body grid contains 6376292 grid points. Simulations were run at experimental conditions at multiple angles of attack for fully laminar, transitioned and fully turbulent flows, all which saw unsteady separated flow at all angles of attack. The laminar case saw large eddies shed off the trailing edge, while the transitional and turbulent cases exhibited a separation region towards the trailing edge, but with no eddies present. 3D simulations were also conducted for Reynolds numbers of 60,000, 100,000 and 460,000 to compare results with the experimental data. It was observed that the higher the Reynolds number, the closer the two sets of results are. However, at lower Reynolds numbers, where a Mars rotorcraft would be operational, the trends deviated which may be attributable to the transitional flow and separation bubbles that occur at lower Reynolds numbers. The flow field near the leading edge of the blades at 75% span revealed a steady thin separated flow region which was marginally thicker for the laminar case. For both cases again, the 3D and rotational effects produced a radial outflow in the separated regions in proximity to the blade surface which spreads from the root to the tip of the blade and is then absorbed by the vortex. Ammoo & Awal [7] investigated the flow characteristics of a RC helicopter main rotor with the aim of using wind tunnel flow visualisation methods to visualize vortex interaction of rotor blades. They utilized a smoke flow visualisation method over the two-bladed main rotor of a Hirobo-Falcon 505 which uses a NACA 0014 aerofoil. The helicopter was fixed to a test rig complete with an electric motor attached to a drive shaft which was connected to the rotor head gear system. A smoke generator was used to provide white smoke, and the helicopter was place in front of a black background. SolidWorks was used to simulate the conditions of the experiment for comparison. Testing for different sections of the blade span in a hover configuration, the flow exhibited different characteristics at each radial point. In the centre of the main rotor around the hub the smoke was in a relatively calm state and moved outwards from the hub passing through 55% of the radial span, where it arched downwards. As the arching flow approached the 75% radial point, the flow changed direction and became straight normal to the blade. The lower velocity of the air at the hub and root region of the blade does not have a strong effect on the flow, and it generally takes the shape around the solids in its proximity. Similarly, when the smoke generator was moved to the outboard portion, above blade tip, the smoke also passed through the disk towards the 75% point adjusting into straight downward flow. When smoke was released at the mid-span, the flow passes through the blade completely straight; this agrees with theory, given that the middle portion of a rotor blade plays the crucial role of generating most of the lift and thrust.

In the present article, we investigate using ANSYS FLUENT computational fluid dynamics [8], the turbulent aerodynamic performance of the blade configuration in the Mars Ingenuity quadcopter design. A detailed rotor blade model for CFD analysis has been developed for flow behaviour around the rotor blades in Mars atmospheric conditions. Data has been extracted from the Mars 2020 mission and the Mars Ingenuity Helicopter as a baseline. A 3D model using SolidWorks is imported into Ansys Fluent. The geometry of the rotor blade model complies with the prototype and extensive simulations are described for contour plots and flow vectors visualizing the rotor blade flow regime, with a focus on vortex effects and performance in the Mars atmosphere. We study the complex flow fields associated with generating lift through the quadcopter rotor blade rotation and also address the unsteady airflow around the rotor disk leading to instabilities such as blade-vortex interactions and retreating blade stall. Furthermore, future areas for investigation including blade twist and control aspects are also outlined.

2. Mars Ingenuity Helicopter Details

The Mars Ingenuity helicopter was designed and operated by NASA's Jet Propulsion Laboratory (JPL) (managed by California Institute of Technology, Caltech), with research conducted from NASA's Ames Research Center and manufactured by AeroVironment, Inc. Ingenuity's first flight on Mars was April 19th 2021, and although only scheduled for 5 flights, it remained fully operational until January 18th 2024 completing a total of 72 flights with a cumulative flight time of 2 hours 8 minutes and 55 seconds. Development of the next generation of Mars rotorcraft is currently undergoing, and Ingenuity serves as a perfect benchmark for future designs. Mars Ingenuity (Fig. 1) is a small and lightweight coaxial counter rotating (4-blade) helicopter with a mass of 1.8 kg and a rotor disk diameter of 1.21 m designed as a proof-of-concept technology demonstrator. The craft is powered by a single lithium-ion battery and recharged using the solar array above the rotor system. Along with the battery, the avionics hardware, and Electronics Core Module (ECM) are kept at optimum temperature via a thermal management scheme where the Helicopter Warm Electronics Box (HWEB) serves as the outer layer providing insulation and further environmental protection from contaminants. The HWEB is constructed from a composite frame wrapped with a polyamide film membrane; optical windows on the bottom of the box provide viewing space for navigational cameras and sensors. Connected to the top of the HWEB frame and bonded to the mast tube, is the moulded composite landing gear interface plate providing the clevis for each deployment hinge, latch, spring-loaded pawls, and the damper/flexure mechanism. The composite deployable landing legs (and feet) are connected via the flexure/damper mechanism with an overall base footprint of 0.33 m^2 proving a stable base to reduce the risk of tip-over.

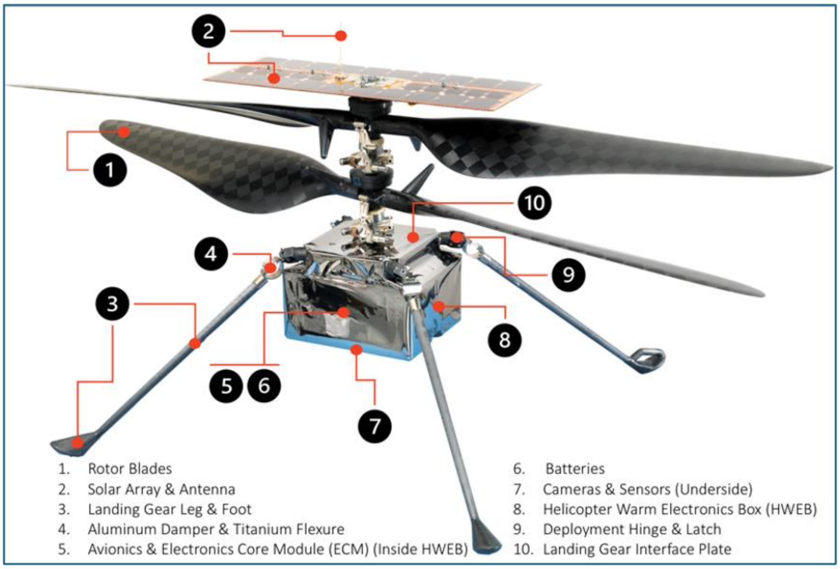

Fig 1: Mars Ingenuity Helicopter (courtesy-NASA JPL, USA)

Ingenuity's rotor system (Fig. 1) consists of four blades, two rotor hubs, the main swashplate assembly, control linkages, servo actuators (and feedback system), upper and lower propulsion motors and associated electronics [9]. The counter rotating blades are spaced apart approximately 8% of the rotor disk diameter with operational speeds of up to 2800 rpm. Depending on the local density, the rotor speed is fixed for the flight duration and controlled using the swashplates, with 22° range of collective control and range of ±10° for in cyclic control. A series of three aerofoils were selected and optimised based on the requirement for operating conditions at ultra-low Reynolds numbers, with a fourth interface tube type foil to form the root between the first and second stations of the blade. The outboard portion of the blade from station 4 at approximately 75% of the span uses the CLF5605 aerofoil. This aerofoil was adapted from AeroVironment's previous high altitude propeller designs but with an adjusted camber line for use with higher lift coefficients.

3. Rotorcraft Aerodynamics & Performance Aspects

The lifting capability of the main rotor is directly related to the angle of attack ($\alpha°$) of the rotor blade and the local dynamic pressure ($0.5\rho V^2$). The position of the rotor blade is defined by the azimuth angle ($\psi°$), which when the blade is pointed downstream is equal to zero. In hover (Fig. 2a) the velocity variation along the span of the blade is azimuthally axisymmetric and radially linear (Leishman [10]); the flow velocity at the hub is zero and the maximum velocity and maximum Mach number is at the tip of the blade (Eq. 1) (Eq. 2), where Ω*(rad/s)* is the rotor rotational frequency, *r(m)* is the disk radius, and *a(m/s)* is the speed of sound. At any blade section (element), the velocity of the surrounding airflow is proportional to the square of the distance from the rotational axis. The average thrust generated by the rotor is dependent on the square of the rotor tip velocity, $V^2_{tip} \infty T$. Similarly, the rotor power is dependent on the cube of the rotor tip velocity, $V^3_{tip} \infty P$. During forward flight (Fig. 2b) the freestream velocity component, $V_\infty (m/s)$, is added or subtracted from the rotational velocity at each blade section (Eq. 3); the velocity distribution along the span of the blade remains linear but is no longer axisymmetric and the magnitude of which varies with respect to the azimuth angle.

$$V_{tip} = \Omega r \tag{1}$$

$$M_{tip} = \frac{V+V_{tip}}{a} \tag{2}$$

$$V_{tip} = \Omega r \pm V_\infty sin\ \psi \tag{3}$$

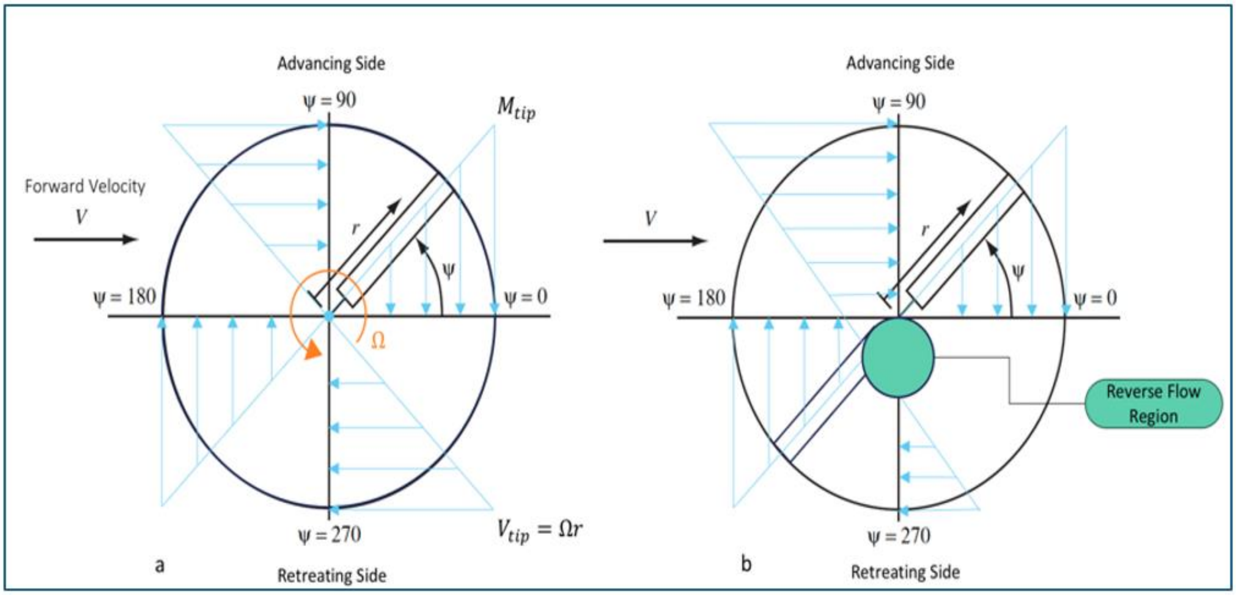

Fig 2: (a) Symmetry of lift in hover (b) dissymmetry of lift in forward flight of the helicopter main rotor.

Rotorcraft are designed to spend a considerable amount of time in hover and operate efficiently; the leading purpose of the main rotor is to generate sufficient lifting force in opposition to the weight of the aircraft. In forward flight a propulsive force is required to overcome drag achieved by the tilting the main rotor plane forward in conjunction with increasing the thrust – this combination ensures that the vertical thrust component (lift) remains equal to the aircraft weight. Referring to Fig. 2b in forward flight the velocity field is asymmetric which is maximum on the advancing side of the rotor disk and minimum on the retreating side, therefore the blade air loads, and the local dynamic pressure become periodic primarily at the rotational speed of the rotor, as noted in Leishman [10]. This causes blade flapping resulting in the tilting of the rotor disk, which is compensated for with cyclic control inputs to change the magnitude and phasing of the $\mathbf{1/rev}$ lift forces over the disk. The aerodynamic performance of the rotor is determined by initially evaluating the lift and drag characteristics of the individual aerofoil sections, from which the thrust and power can be derived. These coefficients are the scaled descriptions of the section and vary with the angle of attack ($\alpha°$), where $L(N)$ is section lift, $D(N)$ is section drag, ρ is density, $V\ (m/s)$ is velocity and $c(m)$ is the section chord.

$$C_l = \frac{L}{0.5\rho V^2 c} \tag{4}$$

$$C_d = \frac{D}{0.5\rho V^2 c} \tag{5}$$

The power required for rotor hover comprises of induced power, which represents the energy dissipated in the rotor wake due to the generation of thrust, and profile power, which represents the energy lost to drag forces acting on the rotor blade sections.

$$P = \kappa T = \sqrt{\frac{T}{2\rho A}} + \rho A_b V_{tip}^3 \frac{1}{8} C_{d(mean)} \tag{6}$$

Here $P\ (W)$ is rotor power, $T\ (N)$ is rotor thrust, $A\ (m^2)$ is the area of the rotor disk, $A_b\ (m^2)$ is the total area of the blades, and $V_{tip}\ (m/s)$ is the blade tip velocity. The induced power factor (κ) is the actual induced power to the ideal induced power ratio – typically $\kappa = 1.2$ in hover and $\kappa = 2$ for forward flight. The profile power is characterised by mean drag coefficient ($C_{d(mean)}$) therefore the rotor blade stall is reflected by this value and is proportional to the blade loading (Eq. 7).

$$\frac{C_{d\,(mean)}}{6} \cong \frac{C_T}{\sigma} = \frac{T}{\rho A_b V_{tip}^2} \tag{7}$$

The rotor solidity (σ) (Eq. 8) is defined as the ratio of the total rotor blade area and the total rotor disk area and gives a measurement of how densely the rotor blades are packed within the disk. The solidity varies with the number of blades (N_b) or the aspect ratio (AR). A higher solidity can increase lift capabilities but may also increase drag, requiring more power to drive the rotor, conversely a lower solidity will reduce drag and lessen power requirements but lift performance will be compromised.

$$\sigma = \frac{A_b}{A} \tag{8}$$

The blade loading (C_T/σ) of the rotor is constrained by stall conditions, with the maximum or design value dictating the necessary blade area or tip speed.

$$\frac{P}{T} = \kappa\sqrt{\frac{T}{2\rho A}} + V_{tip}\frac{C_{d(mean)}}{8C_T/\sigma} \tag{9}$$

As a result, low disk loading (T/A) and higher aerofoil C_l/C_d lead to a reduction in required power. The impact of lower air density increases induced power and augments profile power due to the influence of the Reynolds number on the drag coefficient. To minimise the blade area, a higher tip speed is necessary. The efficiency of a rotor in hover can be measured by the Figure of Merit (FM) (Eq. 10), which is *ratio of the ideal and actual hover power required*. The FM approximates the profile power to induced power ratio and is typical used in comparisons at fixed disk loading. The FM for Mars Ingenuity increases with thrust as the induced power increases – once stall is reached the induced power increase where the FM drops off. The aerofoil drag coefficient increases at a lower Reynolds number resulting in an increase in profile power. A small terrestrial helicopter will have a relatively small FM, but the lower density on Mars means that the induced power is high therefore the efficiency of the rotor in hover is good, although this means that the required power is high, as noted by Johnson et al. [11].

$$FM = \frac{P_{ideal}}{P} = \frac{T\sqrt{\frac{T}{2\rho A}}}{\kappa T\sqrt{\frac{T}{2\rho A}} + \rho A_b V_{tip}^3 \frac{1}{8} C_{d(mean)}} \tag{10}$$

4. Governing Equations

CFD is a subdivision of fluid mechanics which deploys numerical methods and algorithms to analyse and solve problems involving fluid flow based on the fundamental equations– the continuity and momentum conservation equations, also known collectively as the Navier-Stokes equations. The conservation of mass is given as Eqn. 11. Eqn. 12 gives the conservation of momentum, where ρ (kg/m^3) is density, $\frac{\partial v}{\partial t}$ is representative of the speed variation over time (of the fluid), the $v\nabla v$ term is indicative of both fluid speed and direction, ∇P is the pressure change within the fluid, ρg is the buoyancy force representing the external forces acting on the fluid, and finally. The diffusion term $\nabla^2 v$ is defined by the viscosity stress acting on the fluid.

$$\frac{\partial \rho}{\partial t} + \nabla \rho v = 0 \tag{11}$$

$$\rho\left(\frac{\partial v}{\partial t} + v\nabla v\right) = -\nabla P + \rho g + \mu \nabla^2 v \tag{12}$$

To simulate turbulent flow, the $K-\omega$SST model was selected for this investigation. One of the main reasons for its popularity is the ability to predict separation and reattachment better when compared to the $K-\varepsilon$ (k-epsilon) and the standard $K-\omega$ (k-omega) models. The SST model is an improvement of the standard $K-\omega$ model which blends aspects of the $K-\varepsilon$ model. The objective of the SST model is to mitigate the sensitivity to free-stream conditions inherent in the standard model by considering the transport of turbulence shear stress. This model accurately predicts the flow separation over smooth surfaces in open flow scenarios which is not a capability that other two models have on their own. The standard $K-\omega$SST model obtains turbulence specific energy (k) and the specific dissipation rate (ω) from the transport equations given as Eqn. 13 and Eqn. 14, where G_k is the turbulence kinetic energy generated due to mean velocity gradients, G_ω is the generation of ω, Γ_k and Γ_ω denote the effective diffusivity of k and ω, Y_k and Y_ω indicate the dissipation of both k and ω due to turbulence, S_k and S_ω are user defined source terms and finally, G_b and $G_{\omega b}$ account for buoyancy terms.

$$\frac{\partial(\rho k)}{\partial t}(\rho k) + \frac{\partial}{\partial x_i}(\rho k u_i) = \frac{\partial}{\partial x_j}\left(\Gamma_k \frac{\partial k}{\partial x_j}\right) + G_k - Y_k + S_k + G_b \tag{13}$$

$$\frac{\partial}{\partial t}(\rho\omega) + \frac{\partial}{\partial x_i}(\rho\omega u_i) = \frac{\partial}{\partial x_j}\left(\Gamma_\omega \frac{\partial \omega}{\partial x_j}\right) + G_\omega - Y_\omega + S_\omega + G_{\omega b} \quad (14)$$

The effective diffusivities are defined as $\Gamma_k = \mu \frac{\mu_t}{\sigma_k}$ *and* $\Gamma_\omega = \mu \frac{\mu_t}{\sigma_\omega}$ where σ_k and σ_ω are the associated turbulent Prandtl numbers. Combining the turbulence specific energy and dissipation rate we have the turbulent viscosity, $\mu_t = a^* \frac{\rho k}{\omega}$. The a^* term causes a low Reynolds number correction by damping the turbulent viscosity and is calculated by using the following equation:

$$a^* = a_\infty^* \left(\frac{a_0^* + Re_t/R_k}{1 + Re_t/R_k}\right) \quad (15)$$

Here $Re_t = \frac{\rho k}{\mu\omega}$, $R_k = 6$, $a_0^* = \frac{\beta_i}{3}$, $\beta_i = 0.072$. For the $K-\omega$SST model, a blending function is implemented between the $K-\varepsilon$ and $K-\omega$ models which limits the turbulent viscosity. This is done so that the turbulent shear stress transportation can transpire between the freestream and the wall bound flow. The modified turbulent viscosity is given as:

$$\mu_t = \frac{\rho k}{\omega} \frac{1}{max\left[\frac{1}{a^*}, \frac{SF_2}{a_1\omega}\right]} \quad (16)$$

5. Ansys Fluent CFD Simulations

In this section we focus on the CFD simulation of the rotating aerofoils optimised for the second generation of Mars helicopters. A baseline rotor blade geometry was modelled using SolidWorks from data obtained in current literature and imported into Ansys Fluent for CFD analysis. It should be noted that the academic version of Fluent comes with a computational cell restriction and limits the user to 512K mesh elements, and so any mesh generation is capped.

5.1. Rotor Blade Geometry Modelling

There are currently three proposed conceptual designs for future Mars rotorcraft proposed following extensive collaborative research from NASA and JPL. The rotor blade for each follows the same planform, with slightly different chord dimensions and thickness. For this study the hexacopter configuration has been selected which is a 4-bladed rotor consisting of five aerofoils. The main useable portion of the blade is $0.64\ m$ in length. It is important to note that the Mars Ingenuity design has 6 rotor hubs (hexacopter) each with 4 rotor blades (see figure 3 and figure 4).

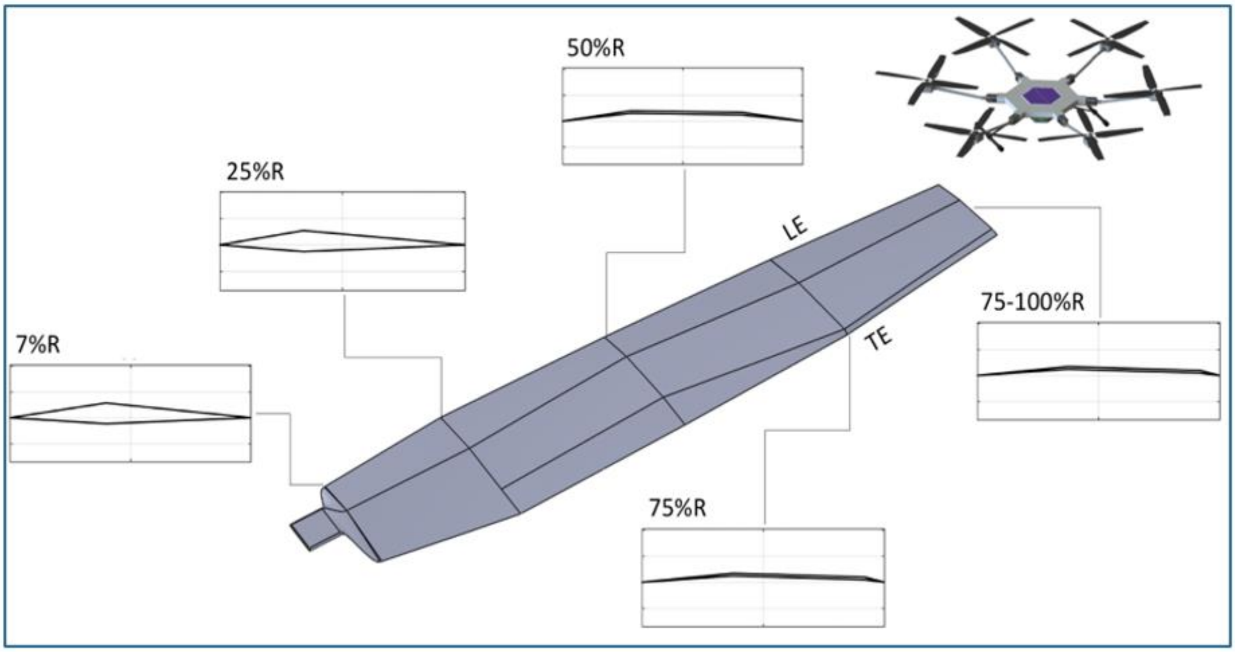

Fig 3: SolidWorks rotor blade model using optimised aerofoils adapted from Koning et al. [12] for the hexacopter configuration of the conceptualised Mars Science Helicopter

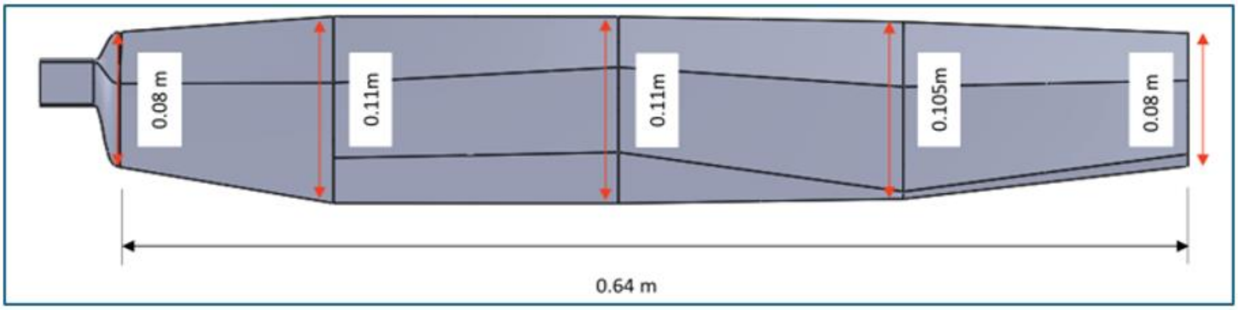

Fig 4: SolidWorks rotor blade model planform featuring chord lengths for each aerofoil section

Scaled dimensionless images of the aerofoils and blade planform were taken from literature and uploaded into an online plot digitiser which generated points based on relative coordinates and input into MS Excel. The aerofoil geometry was then extracted from coordinate plots and sketched in SolidWorks. The chord length at radial stations 7%, 25%, 50%, 75%, and 100% were determined using plot coordinates for the planform. With the aerofoil at each associated radial station sketched, the loft tool was used to create the upper and lower surfaces of the blade from the aerofoil profiles. The 0% - 7% portion of the blade was not specified in any literature and so a simple root-to-hub geometry was modelled as a place holder, however, after initial meshing it was decided to omit this as it created problems with badly shaped elements where the mesh would tend to concentrate around the smaller intricate edges.

5.2. CFD Simulation Cases

Three cases have been selected for simulation of the isolated rotor blades in hover (Table. 1). One of the fundamental considerations in published literature during research and development of a next-generation conceptual design is the rotational speed of the rotor blades in the Martian atmosphere. Discussed previously, due to the incredibly low atmosphere on Mars, the blades are required to spin at higher speed to generate enough lift to fly. Mars Ingenuity has a rotational speed of $\sim 2800\ rpm$ which was sufficient for the mass of the aircraft. Recently JPL have conducted Earth-based tests using the space simulator vacuum to spin Ingenuity's carbon fibre blades up to speeds of $M = 0.95$ at increasing pitch angles to see if they were able to remain intact as the tips reached supersonic speeds. The design cases for this project were selected to investigate the changes in flow characteristics around the conceptual rotor blades with varying rotational speeds and tip velocity. Predominant focus is on the flow visualisation, with attention paid to the thrust capability of the rotor. For this study, it was decided to omit any twist from the blade and conduct the simulation at a collective pitch of 0°; this was purely to create a simple geometry for meshing.

Table 1. MARS Ingenuity Hexacopter Cases Simulated

N (rpm)	$v_{tip}\ (m/s)$	**Atmosphere**
2000	149.7074	Mars
2782	208.2429	Mars
3500	261.9879	Mars

5.3. Computational Flow Domain

Next, we give a description of the initial stages of the simulation setup, focusing on the flow domain and the methods used within Ansys Fluent to capture the flow within a moving reference frame along with the selected boundary conditions.

5.3.1 Multiple Reference Frame (MRF)

The multiple reference frame (MRF) was selected within Ansys Fluent to simulate the rotation of the isolated rotor inside a fluid domain. The MRF model is a steady-state approximation where translational and rotational speeds are allocated to individual cell zones and the flow is calculated using the MRF equations, where the equations reduce to their stationary forms if the cell zone is stationary i.e. $\omega = 0$. Between the rotational and stationary zones is an interface (Fig. 5) at which the local reference frame executes a transformation to calculate the fluxes at the adjoining zona boundary using the zonal flow variables.

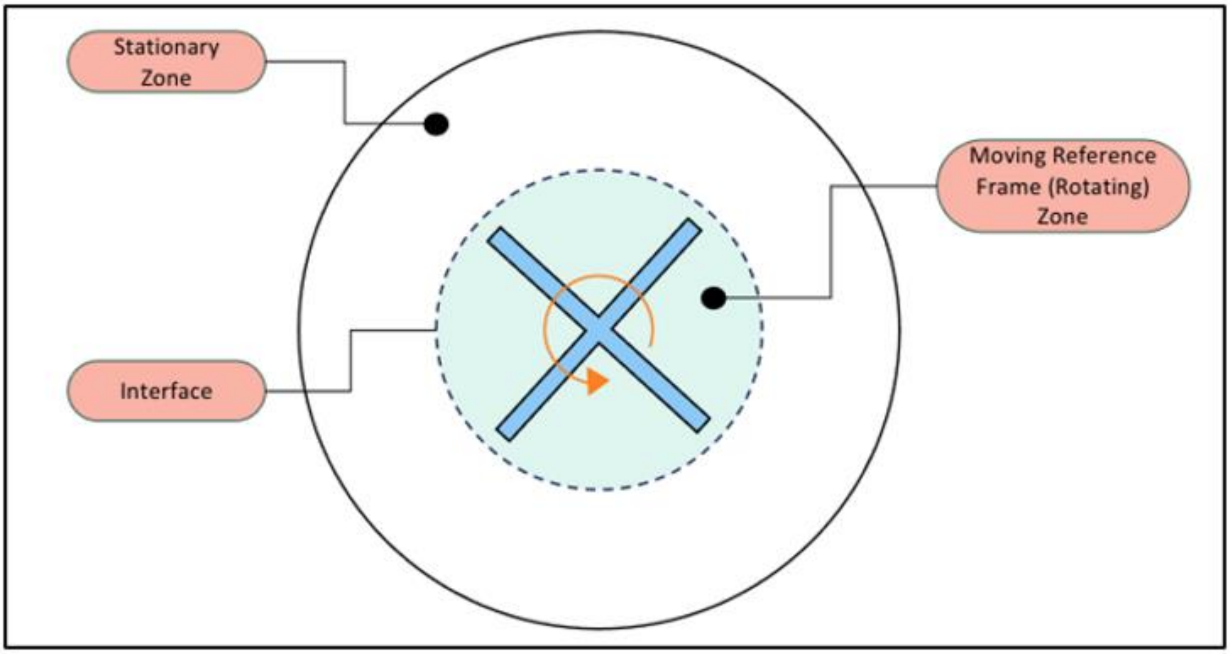

Fig 5: Multiple Reference Frame (MRF) stationary and moving domains with interface

For a coordinate system that is moving with a linear velocity, $\vec{v}_t$ (m/s), and rotating with an angular velocity, $\vec{\omega}$, relative to a fixed (inertial) reference frame – the origin of the moving system is identified as a position vector $\vec{r}_0$ (Ansys, 2021 [8]) (Fig. 6). The unit direction vector $\hat{a}$ defines the axis of rotation giving Eqn:

$$\vec{\omega} = \omega\hat{a} \tag{17}$$

Given the moving frame, the domain is defined so that an arbitrary point is located by position vector $\vec{r}$ from the moving frame origin, which is then transformed into the stationary frame using Eqn. 18, where $\vec{v}_r$ is the relative velocity viewed from the moving frame, and $\vec{v}$ is the absolute velocity viewed from the stationary frame, and finally $\vec{u}_r$ is the velocity of the moving frame relative to the stationary frame.

$$\vec{v}_r = \vec{v} - \vec{u}_r \tag{18}$$

Velocity $\vec{u}_r$ is given as Eqn. 19, where $\vec{v}_t$ is the translational frame velocity and $\vec{\omega}$ is the angular velocity, both of which can be functions of time:

$$\vec{u}_r = \vec{v}_t + \vec{\omega}\vec{r} \tag{19}$$

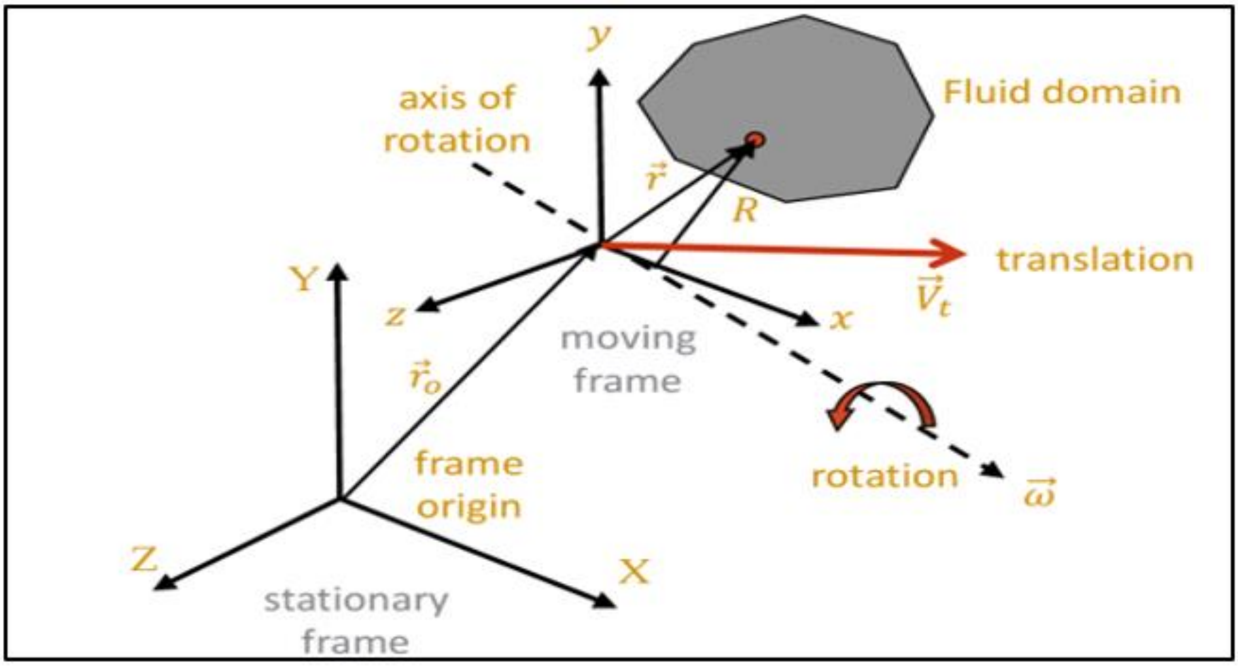

Fig 6: Stationary and moving reference frames in ANSYS FLUENT

By resolving the equations of motion within the moving reference frame, the fluid acceleration is modified by additional terms incorporated into the momentum equation which can be presented by either by formulating the momentum equations using relative velocities or absolute velocities as dependant variables, known as the relative or absolute velocity formulations, respectively. For the MRF model, Ansys Fluent divides the computational domain into sub-domains which can be either rotating, translating, or both with respect to the inertial frame. For each sub-domain the governing equations are written for each sub-domain reference frame. This means that the stationary and translating sub-domain flow is governed by the continuity and momentum equations, while the moving sub-domains are governed by equations for a moving reference frame discussed previously. The boundary interface that divides the sub-domains the diffusion and other terms in the governing equations within one sub-domain necessitate velocity values from the adjacent sub-domain (Fig. 7).

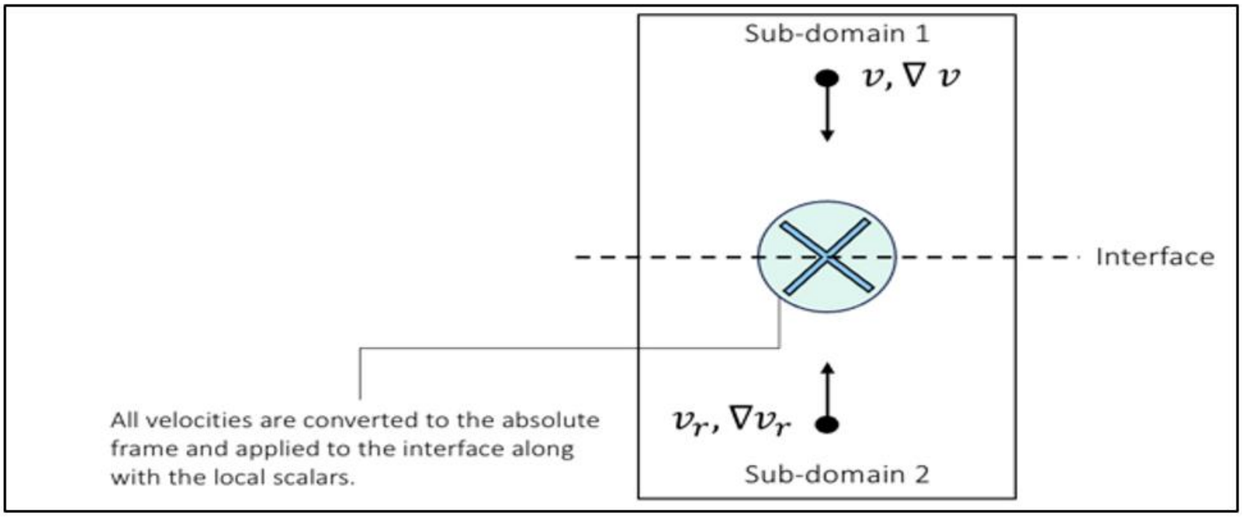

Fig 7: Ansys Fluent subdomains for the MRF model

The continuity of absolute velocity is assured by the solver, denoted as v to provide accurate neighbouring velocity values for the sub-domain under analysis. When employing the relative velocity formulation, the velocities within each sub-domain are calculated relative to the sub-domain motion where the velocities and velocity gradients are converted. The translational velocity is given by Eqn. 19 where the gradient velocity is shown in Eqn. 20. For the absolute velocity formulation, each sub-domains governing equations are with respect to the reference frame of the sub-domain in question, with the velocities being stored within the absolute reference frame. This means that there is no requirement for a specific transformation at the interface. In both formulations, scaler quantities, namely static pressure, static temperature, density, and species mass-transfer etc are obtained from the locally adjacent cells.

$$\vec{v} = \vec{v}_r + (\vec{\omega}\vec{r}) + \vec{v}_t \quad (20)$$

$$\nabla\vec{v} = \nabla\vec{v}_r + \nabla(\vec{\omega}\vec{r}) \quad (21)$$

5.3.2 Domain Geometry

The isolated rotor model was imported into Ansys Design Modeler to create the flow domain (see table 2). This was done with the use of the enclosure tool to first create an enclosure for the rotating domain around the rotor and then a stationary box domain as shown in figure 8. Different size stationary domains were tested but to ensure the stationary domain walls were not influencing the flow around the rotor.

Table 2. Rotating & Stationary Enclosure Dimensions

Rotating Enclosure (Fluid)	
Shape	Cylinder
Alignment	y-axis
FD1 Cushion Radius (> 0)	$0.025\ m$
FD2 Cushion Radius $(> 0) +$	$0.05\ m$
FD2 Cushion Radius $(> 0) -$	$0.05\ m$
Stationary Enclosure (Fluid)	
Shape	Box
FD1 Cushion Radius $(> 0) + x$	$2.2\ m$
FD2 Cushion Radius $(> 0) + y$	$1.25\ m$
FD3 Cushion Radius $(> 0) + z$	$2.2\ m$
FD4 Cushion Radius $(> 0) - x$	$2.2\ m$
FD5 Cushion Radius $(> 0) - y$	$4.45\ m$
FD6 Cushion Radius $(> 0) - z$	$2.2\ m$

Using the Boolean tool the rotor was subtracted from the rotating domain (see table 3), and the rotating domain was subtracted from the stationary domain and preserved, creating the two sub-domains.

Table 3. Boolean Creation for Sub-Domains

	Boolean 1	**Boolean 2**
Operation	Subtract	Subtract
Target Bodies	Rotating Domain	Stationary Domain
Tool Bodies	Rotor	Rotating Domain
Preserve	No	Yes

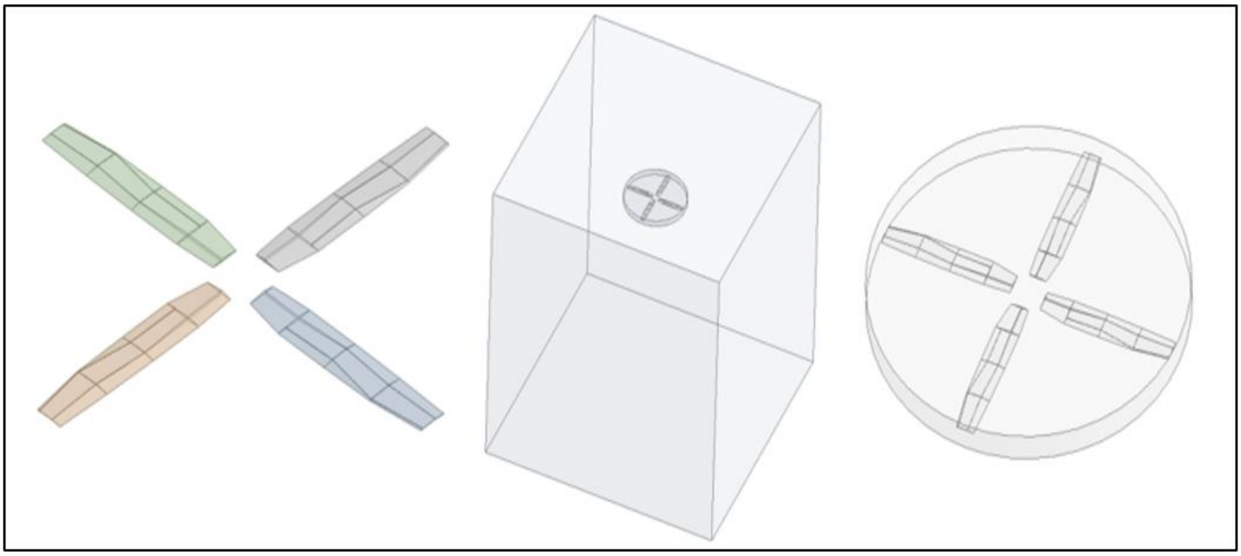

Fig 8: Domain geometry created in Design Modeller for stationery and rotating domains around the rotor blades

5.3.3 Named Selections, Boundary Condition Setup & Reference Values

The named selections for the computational domain are shown in Fig. 9. and were chosen during geometric modelling. The boundary conditions were defined during the setup stage using Fluent (Table 4).

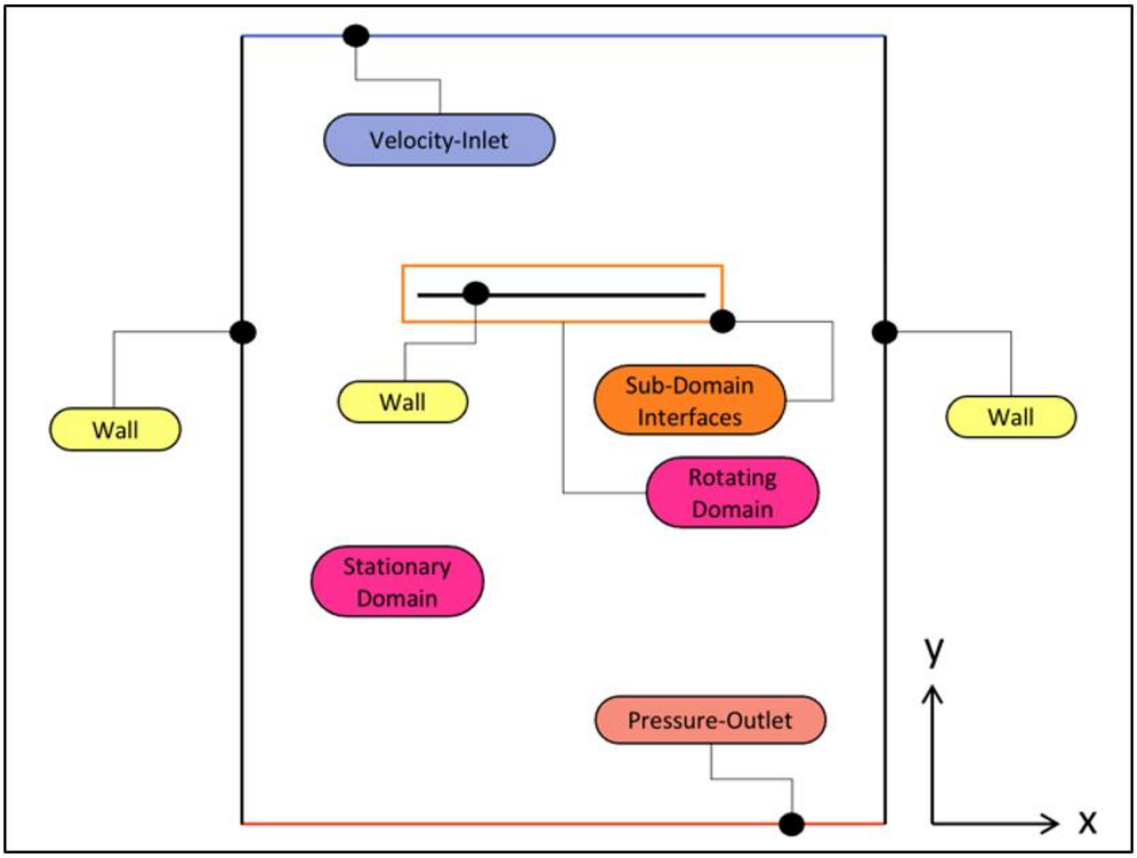

Fig 9: Named selections for the computational domain in Ansys Fluent

Table 4. Named selections and boundary conditions

Named Selection	Boundary Condition	
Inlet	Velocity Inlet	$v = 1\ (m/s)$
Outlet	Pressure-Outlet	$p = 0$
Rotor Blades	Wall	No Slip
External	Wall	No Slip

Reference values used for the simulation are listed in Table 5. The area reference is set to the rotor disk area and velocity is taken as the inlet velocity.

Table 5. Reference values used in Ansys Fluent

Parameter	Value
Area, $A\ (m^2)$	1.61
Velocity, $v\ (m/s)$	1
Pressure, $p\ (Pa)$	716.60
Density, $\rho\ (kg/m^3)$	0.017
Temperature, $T\ (K)$	223.20
Viscosity, $\mu\ (kg/m-s)$	$1.130e^{-5}$

5.3.4 Mesh Construction & Independence Study

The computational space is divided into two sub-domains which is to be discretised into a computational mesh of finite volume elements (see table 6). The mesh is created so that the flow field behaviour can be captured. A mesh independence study was conducted to ensure accuracy of the solution while selecting a mesh density that best balances the trade-off between accuracy and computational power. An initial coarse mesh was constructed (Fig. 10a) consisting of 145805 elements and 29126 nodes. The simulation was run and thrust values recorded. The maximum element size was reduced for each iteration until the difference dropped consistently below 1%, thus ensuring the thrust values would not change with any further mesh adjustments. Local sizing was applied to the rotational domain to create a finer mesh with curvature capture and a growth rate of 1.15 from the default 1.2 representing an increase in the element edge size with each layer of elements (see figure 11). Working within the 512K element limitation the final element count was 498752 with 95447 nodes and a maximum element size of $0.102\ m$ (Fig. 10b-c).

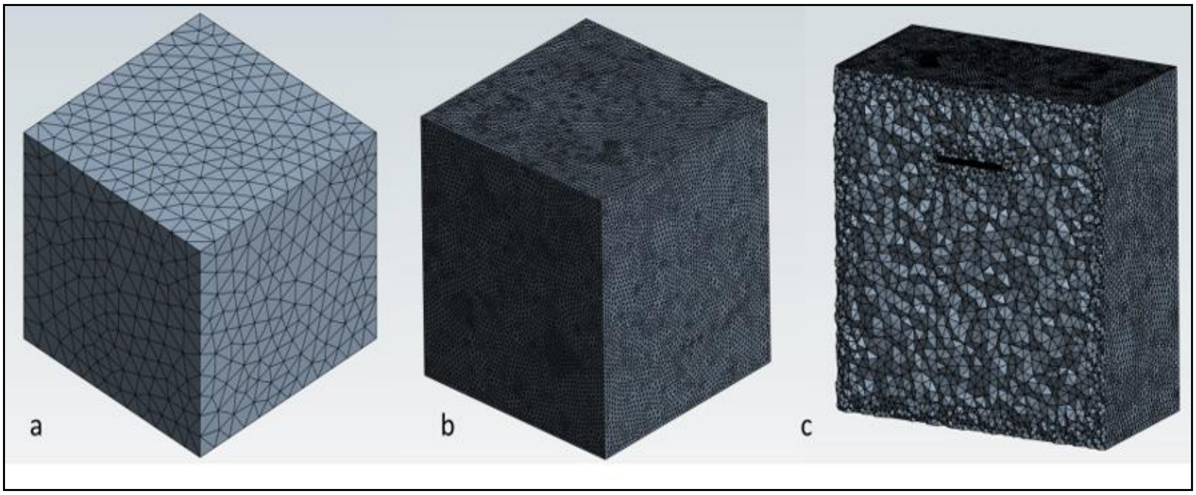

Fig 10: Mesh generation for the computational domain from a) coarse to b) refined to c) final optimized design of 498752 elements.

Table 6. Mesh Independence Study

Elements	Nodes	Thrust (N) at 200th Time Step	Difference (%)
145805	29126	0.94	
158901	32143	0.98	4.25531915

210664	41977	1.04	6.12244898
303318	59523	1.06	1.92307692
498752	95447	1.07	0.94339623

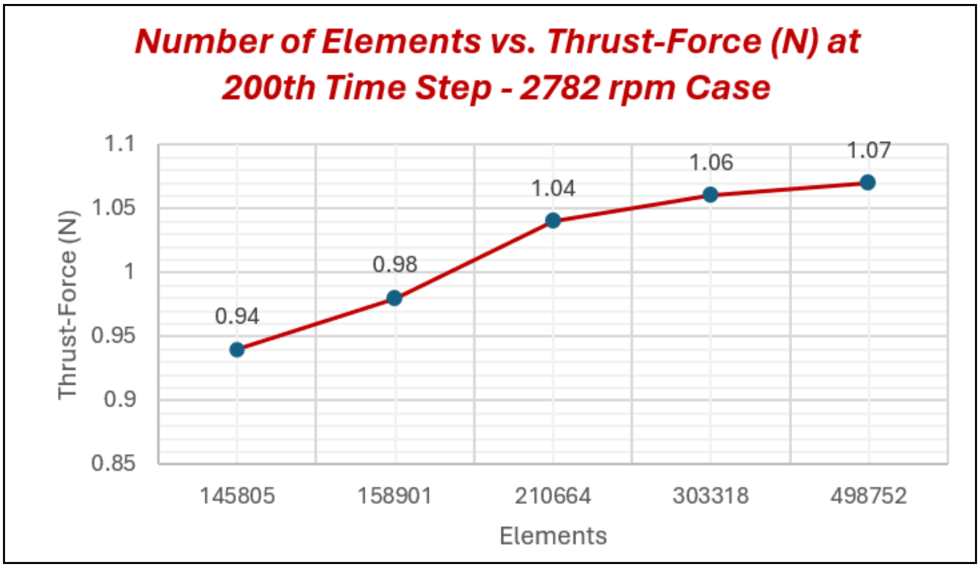

Fig 11: Mesh convergence study – number of elements vs. thrust force (N) at the final (200th) timestep

5.3.5 Computational Setup & ANSYS FLUENT Solution Methodology

Ansys Fluent has several different models and methods to set up a simulation depending on the flow case in question. For this study settings were selected based on information in literature with similar test scenarios, use of the Ansys Fluent Theory Guide, and taking techniques from various tutorial videos available online. ANSYS Fluent uses the Finite Volume Method (FVM) to solve the governing equations of the fluid flow which involved discretising the fluid domain into a series of small, interconnected control volumes (cells) which is then divided into the mesh of volume elements. The governing equations can be expressed using the term ϕ, which represents all scaler quantities of the Navier-Stokes equations and additional properties introduced to the FVM, including turbulent properties. Governing equations then use for example, $\frac{\partial(\rho\phi)}{\partial t}$ which represents the time rate of change of the quantity $\rho\phi$, $div(\rho\phi u)$ represents a divergence of flux for the $\rho\phi u$ term with u being the velocity vector, $div(\Gamma\nabla\phi)$ represents a divergence of the diffusive flux of the quantity $\Gamma\nabla\phi$ of which Γ is the diffusivity coefficient and $\nabla\phi$ is the gradient of the scaler quantity, and finally S_θ is the source sink of the scaler quantity. The initial and most straightforward approach available in the Fluent CFD solver is the first-order upwind scheme. In this scheme the general flow property ϕ in each cell is compared to that of the adjacent cell in the direction of the velocity vector. Consequently, the cells facing the upstream direction, denoted by ϕ_f, will assume the same value as the central cell of the upstream cell. The second-order upwind scheme offers further accuracy and is utilized here. In this approach the cell centre quantities are calculated through the multidimensional linear reconstruction. The SIMPLE (Semi-Implicit Method for Pressure Linked Equations) is a numerical technique for pressure-velocity coupling has been deployed in the present simulations establish an equation for pressure based on momentum and continuity equations, alongside deriving a correction for the velocity field to ensure compliance with the continuity equation.

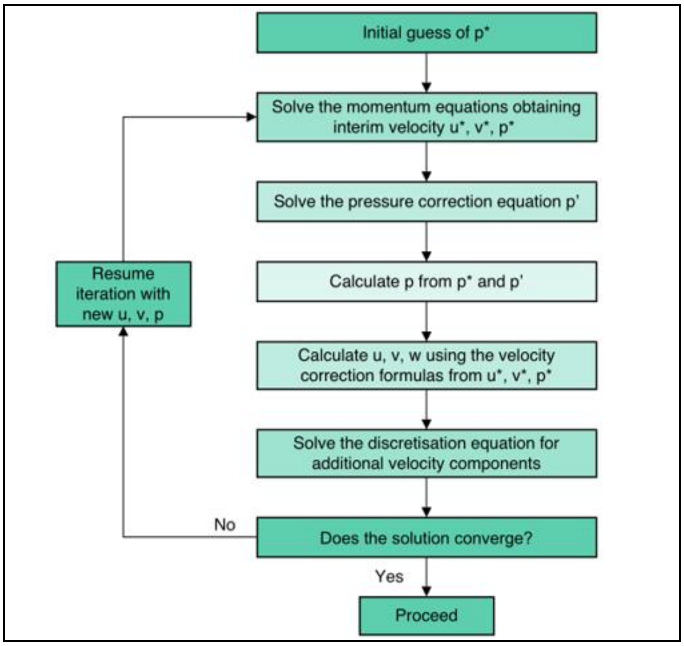

Fig 12: SIMPLE algorithm sequence of operations

Fig. 12 presents the process of the SIMPLE algorithm. To initiate the procedure the pressure field is estimated (p^*) and used to solve the momentum equations.

$$a_e u_e^* = \sum a_{nb} u_{nb}^* + b + (p_P - p_N) A_e \tag{22}$$

$$a_n u_n^* = \sum a_{nb} u_{nb}^* + b + (p_P - p_N) A_n \tag{23}$$

The pressure correction is identified through solving the discretised equation for (p') [8]:

$$a_P p_P' = a_E p_E' + a_W p_W' + a_N p_N' + a_S p_S' + a_T p_T' + a_B p_B' + b \tag{24}$$

Moving forward, the pressure is calculated.

$$p = p^* + p' \tag{25}$$

The components u, v, w are determined using the velocity correction equations.

$$u_e = u_e^* + d_e(p_P' - p_E') \tag{26}$$

$$v_n = v_n^* + d_n(p_P' - p_N') \tag{27}$$

$$w_t = w_t^* + d_t(p_P' - p_T') \tag{28}$$

The penultimate step in the process is to discretise for any other variables with influence on the flow field through fluid properties and/or source terms. The new corrected pressure value at this point can either be reintroduced into the algorithm for further iteration or the solution is complete after convergence. When convergence has been achieved the velocity distribution has been obtained and satisfies the continuity equation. The SIMPLE method in combination with the second order upwind scheme available for pressure-based solvers creates higher levels of accuracy via the multidimensional linear reconstruction approach which computes quantities at the cell faces where the accuracy for cell faces is reached by Taylor series expansion off the cell-centred solution, as noted in (see refs. [13-17]) and is implemented by Eqn. (28):

$$\phi_f, SOU = \phi + \nabla\phi \cdot \vec{r} \tag{29}$$

Here ϕ_f is the cell facin ae, where ϕ is the cell-centred value and $\nabla\phi$ is the associated gradient in the upstream cell with $\vec{r}$ indicating the displacement vector from the upstream cell-centroid to the face centroid, as noted in Daud *et al.* [18] and Bég et al. [19-21] where it has been applied in a variety of applications including turbulent gas turbine blade cooling, peristaltic pump hydrodynamics and green fuel cell enclosure fluid dynamics. The gradient is to be determined for each cell where it will eventually reach a point at which any new maxima or minima are prevented from being introduced. Although there are modifications to the SIMPLE methodology, namely SIMPLER and SIMPLEC, however due to its robustness the SIMPLE method is still deployed as a default solver regularly, specifically in Ansys Fluent, largely due to being established over several decades in various CFD applications proving its reliability.

5.3.6 Additional Settings

Further settings are listed in Table 7. It is recommended that for pressure and momentum in cases where the mesh is not aligned with the flow that the second order upwind scheme is implemented – this is true for the rotating sub-domain and therefore was selected. The turbulent kinetic energy, specific dissipation rate and transient formulation were left as default. A thrust force calculation definition was set up to record thrust against the simulation time for each time step. This was run alongside the residual view port and was used to gauge the level of output fluctuation. Most test runs indicated that the output thrust value settled around a single point after approximately 25% – 50% of the calculation.

Table 7. Additional Settings (Ansys Fluent)

Setting	Selection
Pressure-Velocity Coupling	SIMPLE
Gradient	Least Squares Cell Based
Pressure	Second Order
Momentum	Second Order Upwind
Turbulent Kinetic Energy	Second Order Upwind
Specific Dissipation Rate	Second Order Upwind
Transient Formulation	First Order Implicit
Initialisation	Hybrid
Number of Time Steps	200
Time Step Size	0.005 sec
Max Iterations/Time Step	10

6. ANSYS FLUENT CFD Results & Discussion

Here we present the results of the simulations for the three cases in the form of thrust performance and flow visualisation.

6.1 Rotor Thrust Performance Output

Thrust values for the three cases yielded expected results in that the increase in rotational speed produced more thrust. Emphasis on thrust capabilities have been of high importance during previous research conducted into rotor blade optimisation for Mars powered flight due to the inherent difficulty that comes with the change in atmospheric conditions. As stated in previous chapters the rotor of any rotary-wing vehicle to fly on Mars must spin at extremely high speeds to produce required thrust to fly. Before running the simulation for this investigation, it was unknown what exact thrust output was realistic, however the study of Perez & Natalia [22] documented both experimental and numerical results for a two-bladed rotor in conditions very close to those on Mars. These results were used to gauge whether the results from this study were in the correct range. For rotational speeds from 2000 rpm to 2800 rpm both experimental results and those from using RotCFD, output thrust values between $0.8N$ to $2N$ (see figure 13). The atmospheric pressure associated with results from Perez & Natalia [22] was 1400 Pa. The rotor model used for the current study is not as detailed as the tests conducted by Perez & Natalia [22], as twist has been omitted, so the performance is modified. The CFD results cannot fully capture the rotors' true potential. However, the fact that the present ANSYS FLUENT CFD are in the same range while testing in a lower atmospheric pressure is a positive sign that the unconventional design could surpass current performance outputs (see table 8). The results here prove that *lower rotor speeds are ineffective on Mars*.

Table 8. Rotor thrust output for isolated rotor at varying rpm

Output	$2000\ rpm$	$2782\ rpm$	$3500\ rpm$
Thrust, $T\ (N)$	0.39	1.08	1.57

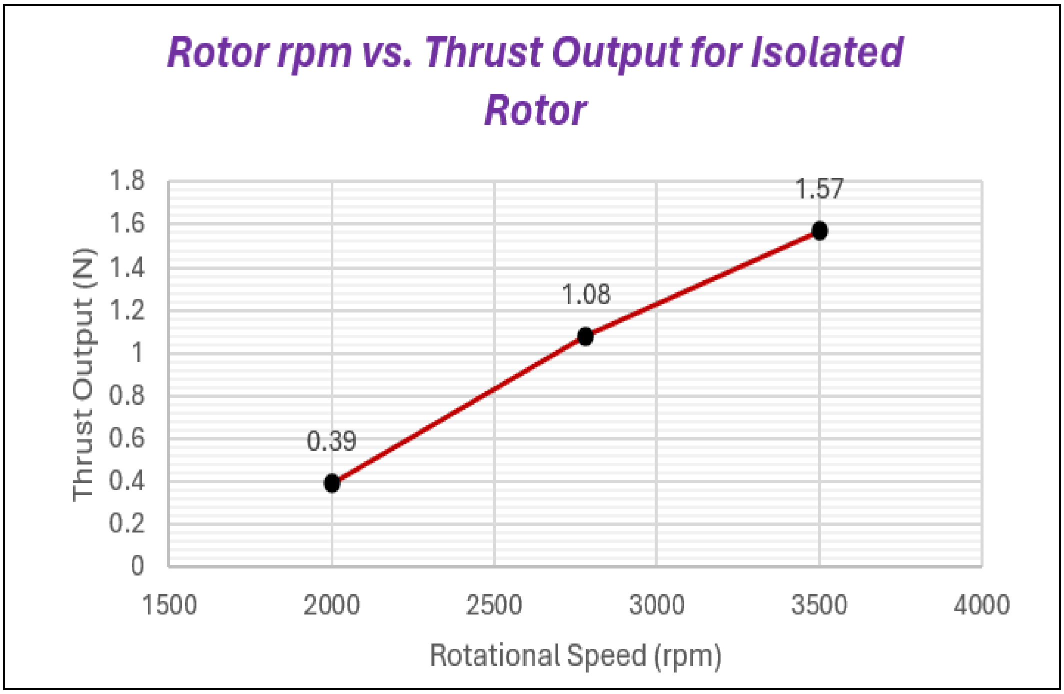

Fig 13: Results for rotational speed (rpm) vs. output thrust (N)

6.2 Flow Visualisation

The following section presents contour plot results for the three cases focusing on velocity, pressure, streamlines, vorticity & turbulent kinetic energy distributions.

6.2.1 Velocity Contours

Fig. 14 below show a snapshot of the computational domain of the isolated rotor in hover at the final timestep. The vertical plane splits the domain through the middle at the centre of the rotating domain; good continuity between the rotational and stationary domain is shown when coloured mapped for velocity magnitude.

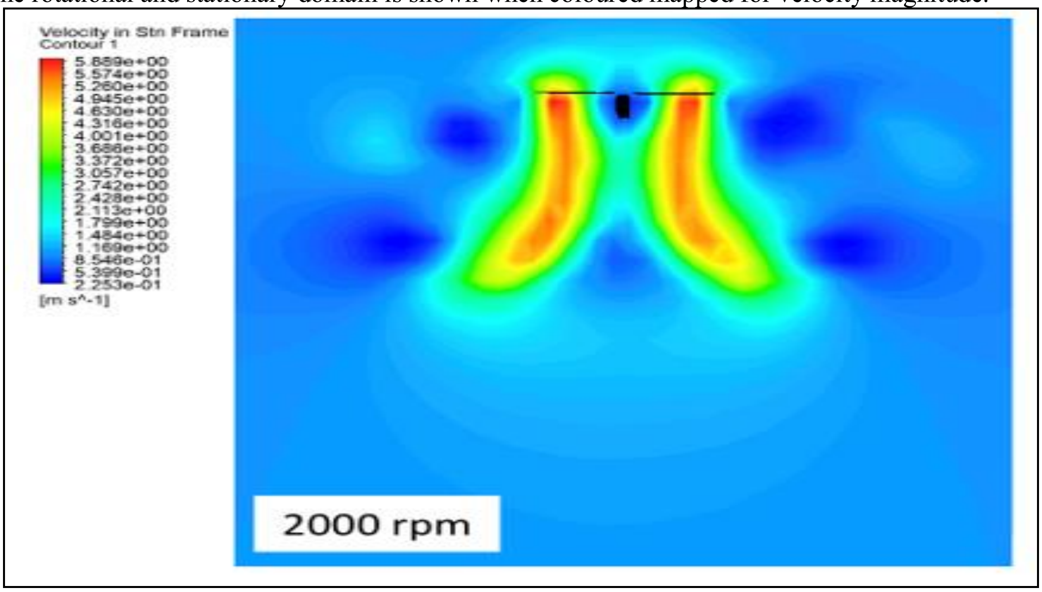

Fig 14: 2000 rpm case – isolated rotor in hover down vertical central plane, velocity contour.

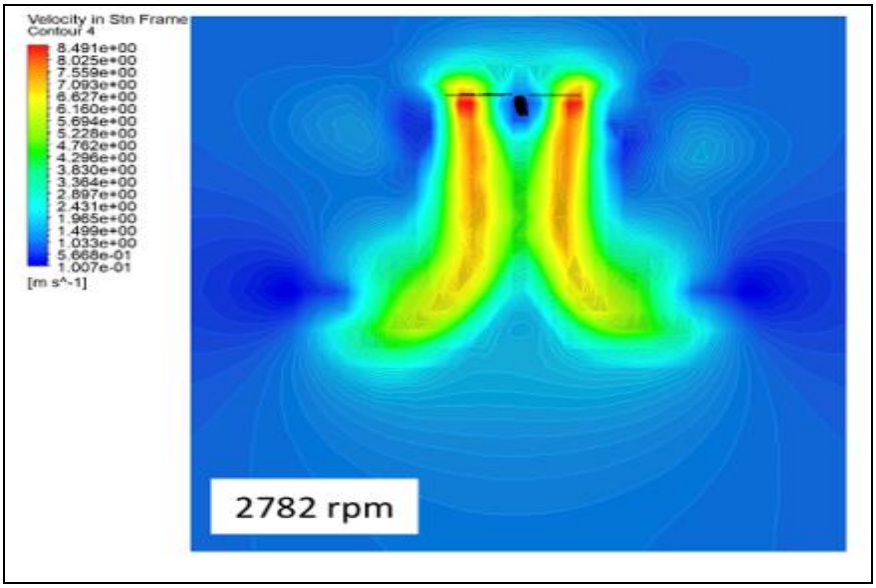

Fig 15: 2782 rpm case – isolated rotor in hover down vertical central plane, velocity contour.

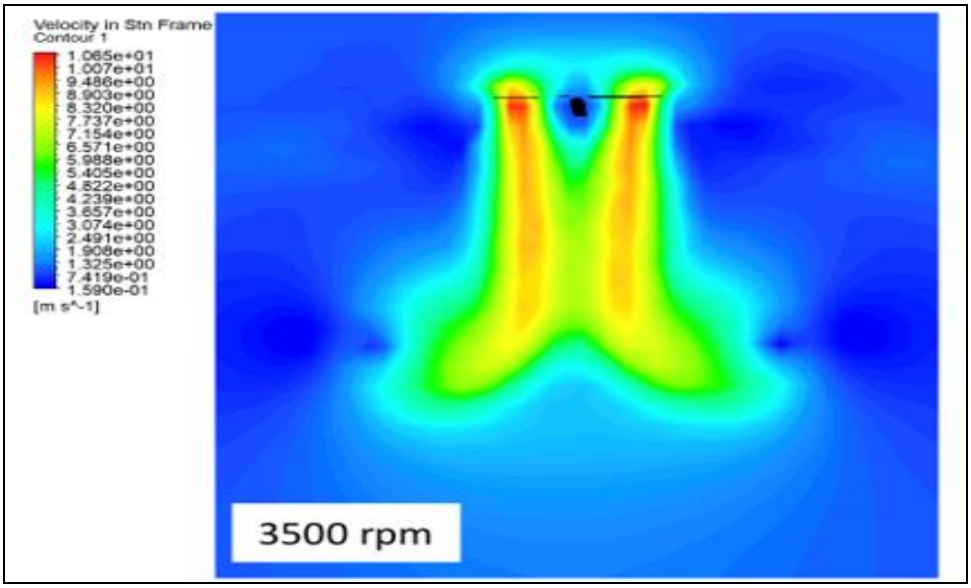

Fig 16: 3500 rpm case – isolated rotor in hover down vertical central plane, velocity contour.

Inspection of Figs 14-16 reveals that flow velocity increases with an increase in rpm, with maximum velocity recorded at 5.9 m/s, 8.5 m/s, and 10.7 m/s respectively. As elaborated in the experimental study conducted by Ammoo & Awal [7] the flow at the 50% – 75% section of the blade exhibits the highest velocity flow almost normal to the blade surface for each case, which equates to the blade section that produced the greatest amount of lift. In *hover* the flow is seen as an *axisymmetric stream tube passing through the rotor disk*. To increase the lift the mass flow rate of air passing through the rotor disk must increase; on Mars this is made more difficult due to the extremely low density of air in comparison to Earth, and therefore the rotor must displace a larger volume of air by increasing the rotational speed to generate the equivalent (on Earth) amount of lift. According to $\dot{m} = \rho AV$, an increase in the mass flow rate, $\dot{m}$ (kg/s) means an increase in the flow velocity with a constant density and rotor disk area. There is no evident lift towards the centre of the rotor at the hub region, justifying the exclusion of hub geometry in the model. For each case, the velocity distribution over the blade span is consistent with theory, in that the blade tips see the maximum velocity which then decreases gradually towards the root

(Fig.17). The blade tip velocity was estimated using Eq. 29 (see table 9), where radius r (m) of the rotor disk is $0.7148\ m$ and the rotational speed is N (rpm):

$$v_{tip} = \frac{2\pi r N}{60} \tag{29}$$

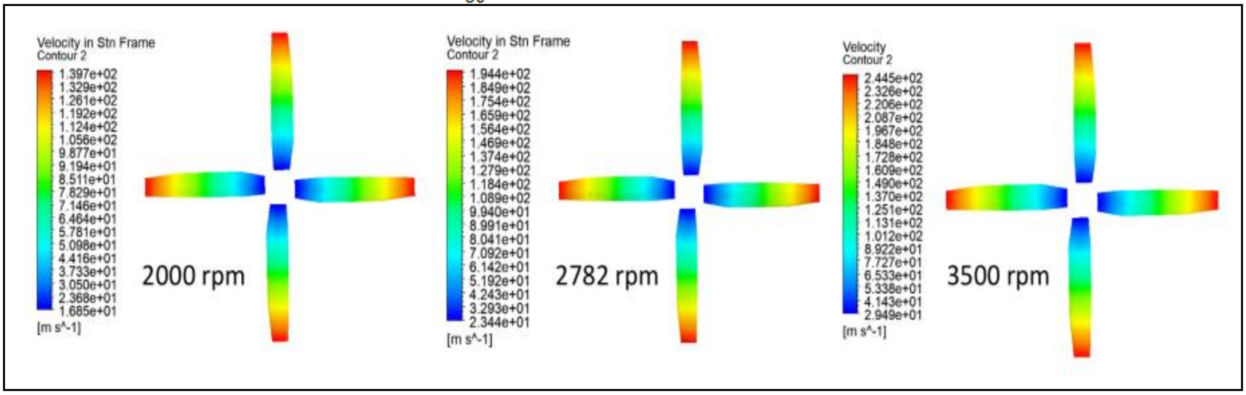

Fig 17: Rotor blade velocity distribution along the blade span for each rotational speed.

Table 9. Estimated vs. Numerical (CFD) Blade Tip Velocity

Rotor Speed (rpm)	Estimated V_{tip} (m/s)	Numerical V_{tip} (m/s)	Difference (%)
2000	149.7074	139.7	6.92
2782	208.2429	194.4	6.88
3500	261.9879	244.5	6.90

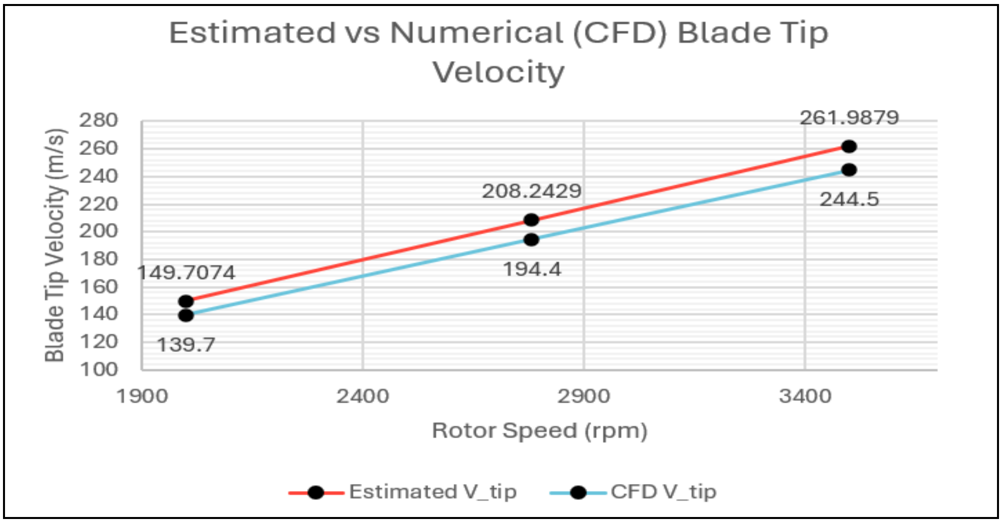

Fig 18: Estimated and CFD results for blade tip velocity (m/s) vs. rotational speed (rpm)

As presented in Fig. 18, there is a slight discrepancy between estimated and numerical results with approximately 7% difference between the two for each case. This could either be down to assumptions made using Eq. 29 which does not account for any contributing factors, or errors in the mesh which effects how the governing equations are calculated.

6.2.2 Pressure Contours

To observe the pressure distribution of the flow field within the computational domain the same section plane was used to intercept the mid-section of the rotating domain.

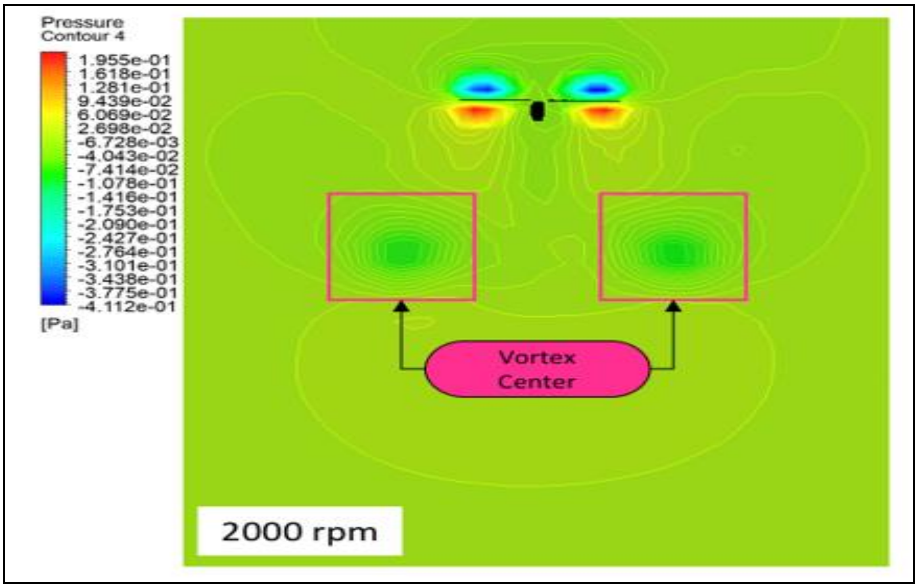

Fig 19: 2000 rpm case – isolated rotor in hover down vertical central plane, pressure contour

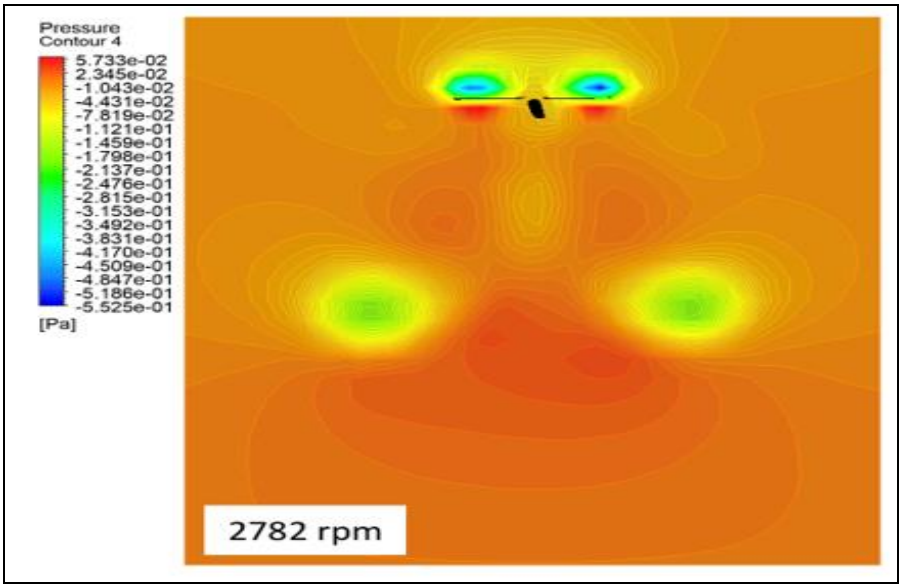

Fig 20: 2782 rpm case – isolated rotor in hover down vertical central plane, pressure contour

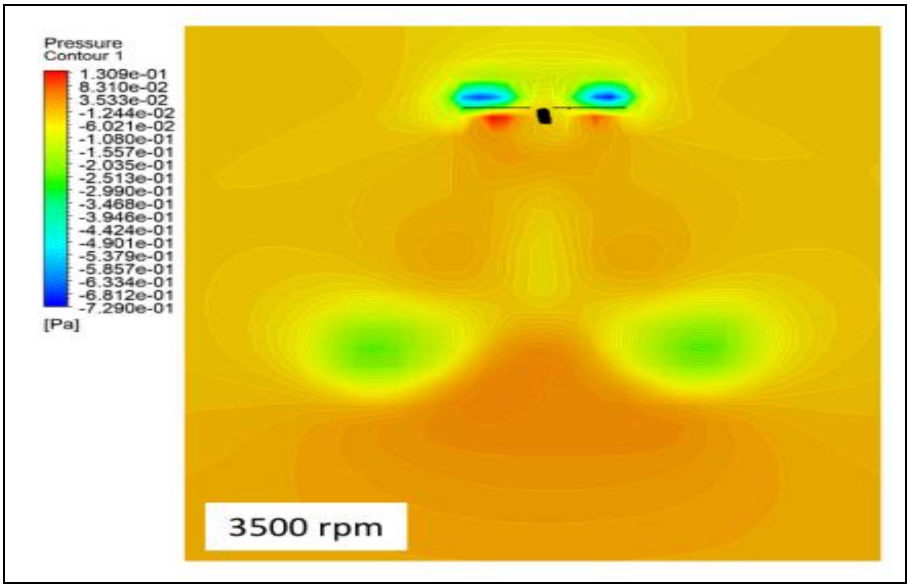

Fig 21: 3500 rpm case – isolated rotor in hover down vertical central plane, pressure contour

Figs. 19-21 presents the pressure contours on this plane. The noticeable difference between pressure values for the regions above and below the rotor is in comparison to the pressure of the surrounding flow and is directly related to Bernoulli's principle, which states that an increase in pressure occurs simultaneously with a decrease in velocity. All the plots are reasonable high-fidelity representations, in which it is evident that both the lower and higher-pressure zones above the rotor are more outboard pertaining to the higher lift portions of the blade. The circular zones of lower pressure downstream of the rotor can be identified as regions of flow circulating within a vortex. Fig. 22-24 present results for pressure on the upper and lower surfaces of the rotor blades for each simulated rotational speed. Expanding on description of the previous pressure contours, the focus is now on the pressure distribution of the two surfaces. All three of the simulated working conditions have a similar trend, with a lower overall pressure on the top (suction) surface and higher overall pressure on the lower surface of each blade.

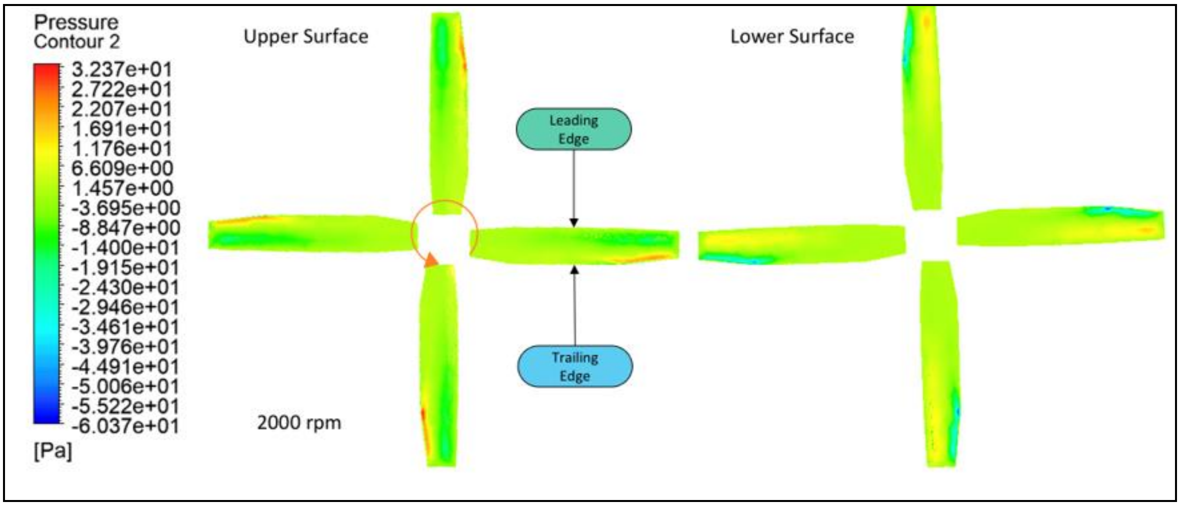

Fig 22: 2000 rpm case – pressure distribution along the radial span of upper and lower rotor blades

This is most prominent on the outboard sections from the mid-point to the tip of the blade. The lower pressure region indicates that the rotor is being sucked upwards by the fast airflow over the top of the blades. This pressure disparity creates a net force on the blade leading to the generation of thrust – a larger pressure difference means more thrust is generated. Unlike conventional aerofoil profiles designs that see a high pressure point at the leading edge, the double-edged plate (DEP) aerofoil that makes up the outboard portions of the rotor blade mitigates the negative effects of stagnation point, such as drag, by promoting almost immediate flow separation. Table 10 documents the minimum and maximum pressure on upper and lower rotor blade surfaces and significant differences are observed at the three rotor speeds.

Table 10. Minimum and maximum pressure on upper and lower rotor blade surfaces

Rotor Speed (rpm)	Minimum Pressure (Pa)	Maximum Pressure (Pa)	Difference (Pa)
2000	-60.37	32.37	92.74
2782	-105.4	55.26	160.66
3500	-200.8	100.3	301.1

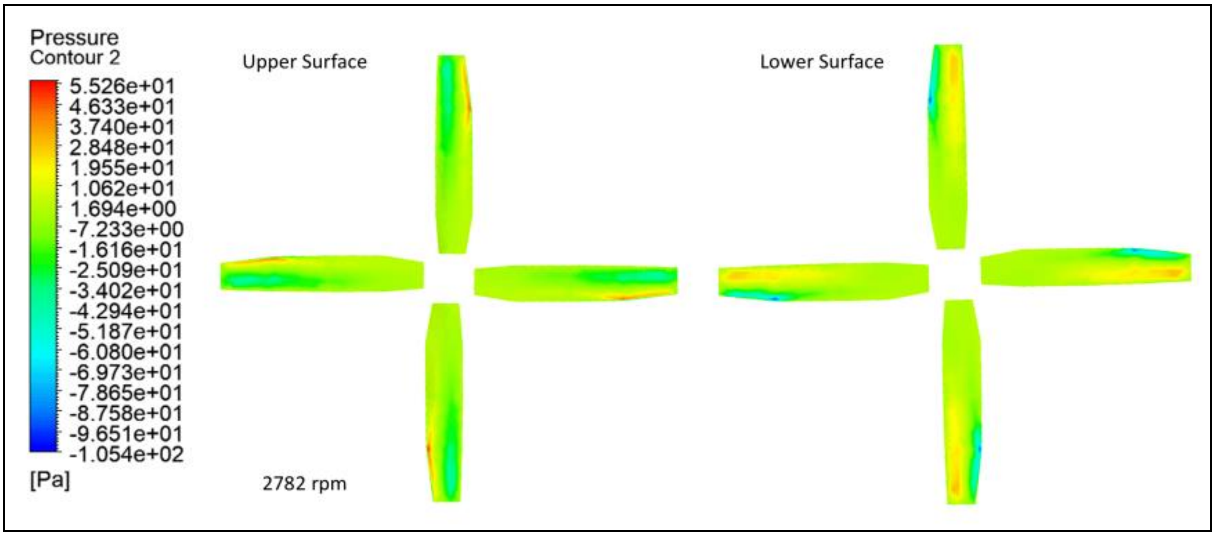

Fig 23: 2782 rpm case – pressure distribution along the radial span of upper and lower rotor blades

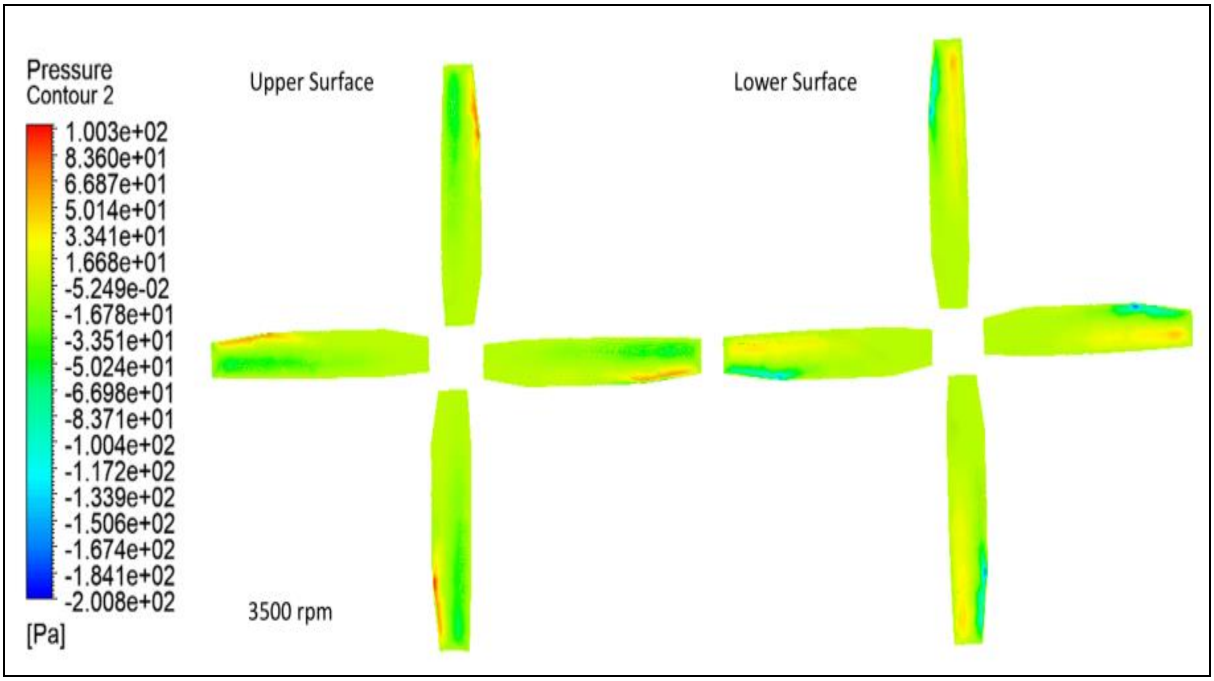

Fig 24: 3500 rpm case – pressure distribution along the radial span of upper and lower rotor blades

The region of high pressure on the top surface of the blade suggests that the flow towards the trailing edge on the outer section of the blade is transitioning to low velocity from the high velocity flow over most of the chord. This could be due to the initiation of the blade tip vortices forming.

6.2.3 Streamlines

The streamlines of the full fluid domain are presented in Fig. 25-27. Each plot uses equally spaced samples with 250 points. Each case shows the propeller rotating at a steady speed drawing the air in from the inlet above. Consistent with Fig. 17, the air inside the rotating domain sees the highest velocity towards the outer perimeter, proceeding to slow once passing through the rotor downstream. The difference in the flow field behaviour around the rotor is apparent, with the $2000\ rpm$ case showing less effect on regions further afield and the $3500\ rpm$ case showing evidence of larger regions of swirling flow.

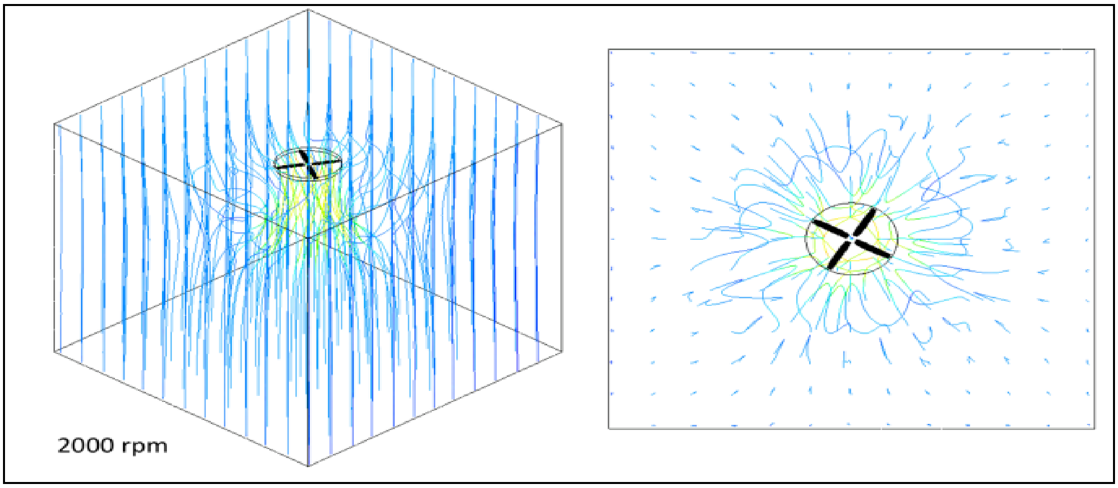

Fig 25: 2000 rpm case – streamlines coloured for velocity of the whole computational domain.

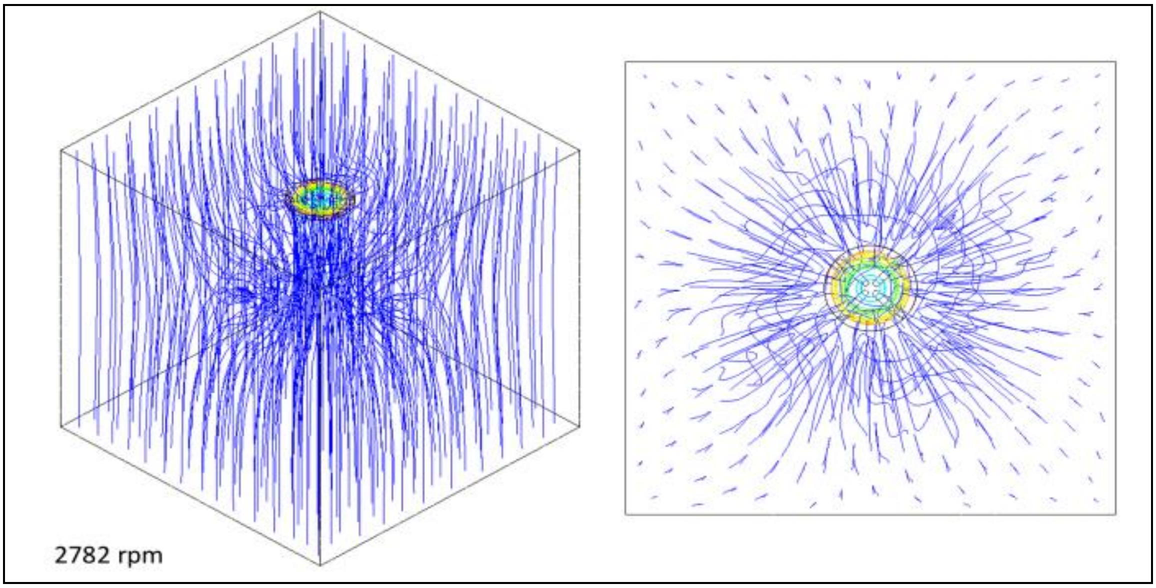

Fig 26: 2782 rpm case – streamlines coloured for velocity of the whole computational domain.

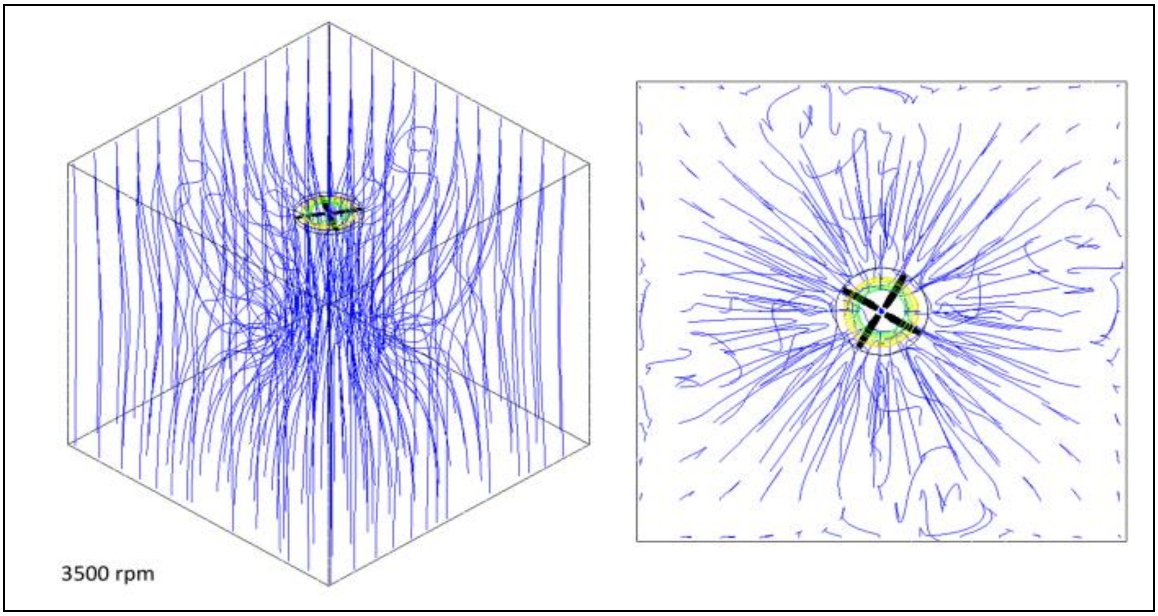

Fig 27: 3500 rpm case – streamlines coloured for velocity of the whole computational domain.

Using the same mid-section plane, Fig. 28-30 visualize the streamlines for all 3 rotor speed cases. The general trend shows the air passing through the rotor normal to the blade and subsequently diverging. The slipstream travels around the rotor meeting the diverging flow and seems to create a vortex region where the flow begins to recirculate. The increase in rotor speed sees this occurrence become more pronounced. Also, note that for the $3500\ rpm$ case the flow behaviour influences a larger area of the fluid domain which is due to the increase in flow activity from the greater amount of thrust and greater mass flow rate through the rotor. In the computational domain there becomes a risk that the flow could be affected by the bounding box walls, although there is no apparent major evidence of this in the present simulations, nevertheless it is something to consider.

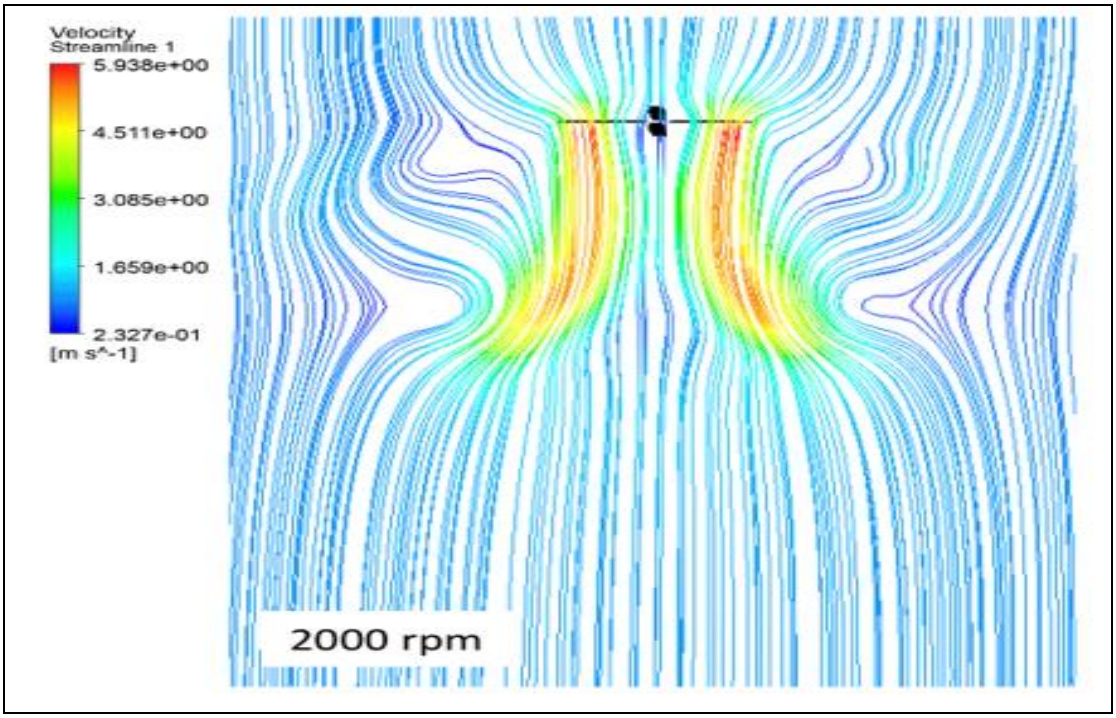

Fig 28: 2000 rpm case – isolated rotor in hover down vertical central plane, streamlines coloured for velocity

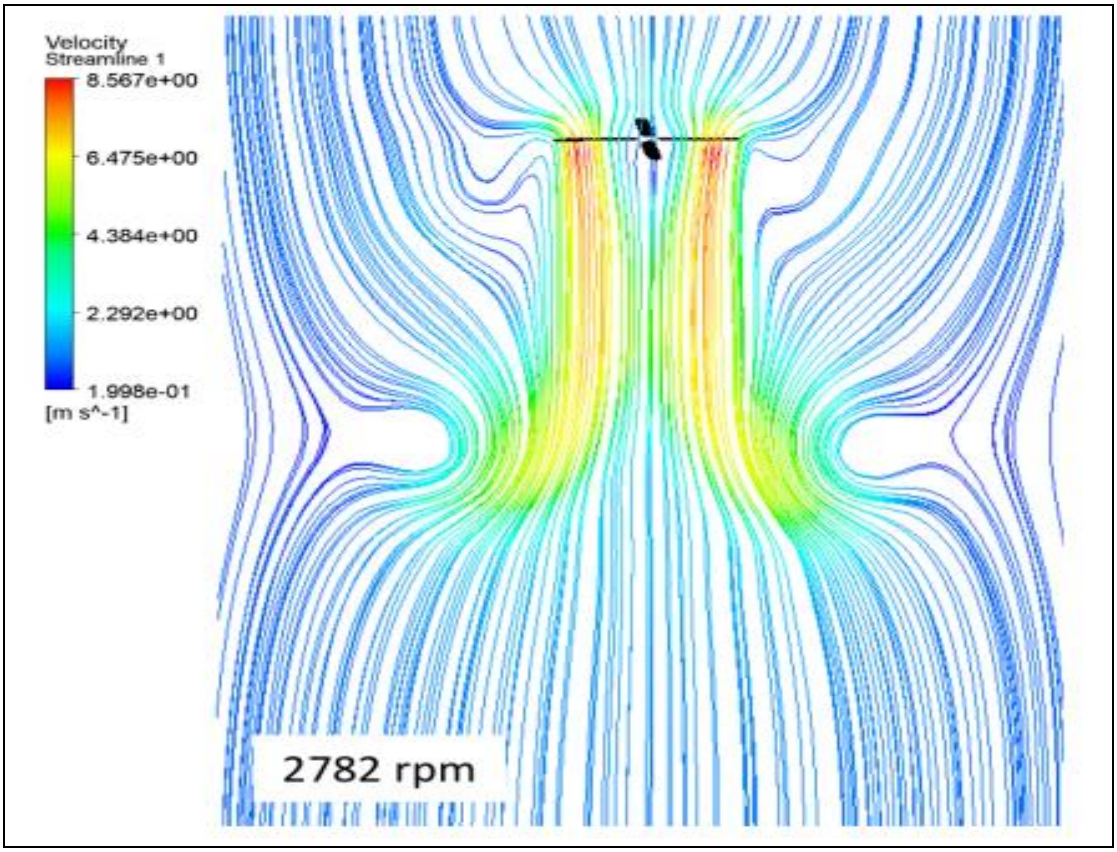

Fig 29: 2782 rpm case – isolated rotor in hover down vertical central plane, streamlines coloured for velocity

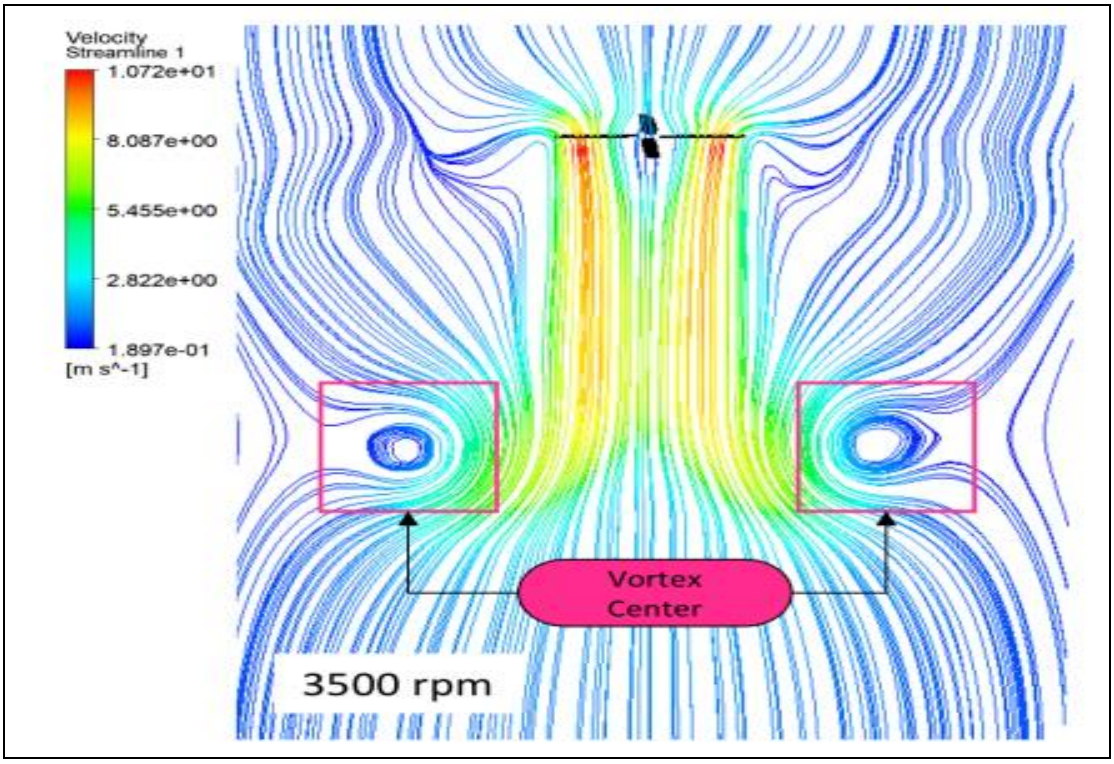

Fig 30: 3500 rpm case – isolated rotor in hover down vertical central plane, streamlines colored for velocity

6.2.4 Vorticity & Turbulent Kinetic Energy

The Q-criterion is a concept used in CFD analysis to identify and visualise regions a fluid flow where vortices are present, providing a quantity measurement of the local vorticity of the flow field. It can be deployed to identify vortex cores and regions of intense vorticity particularly in rotor and propeller wakes. Fig. 31 to Fig.33 display the Q-criterion method coloured for pressure. Each plot was computed for the same level to compare flow activity, focusing on the area directly at the rotor blades.

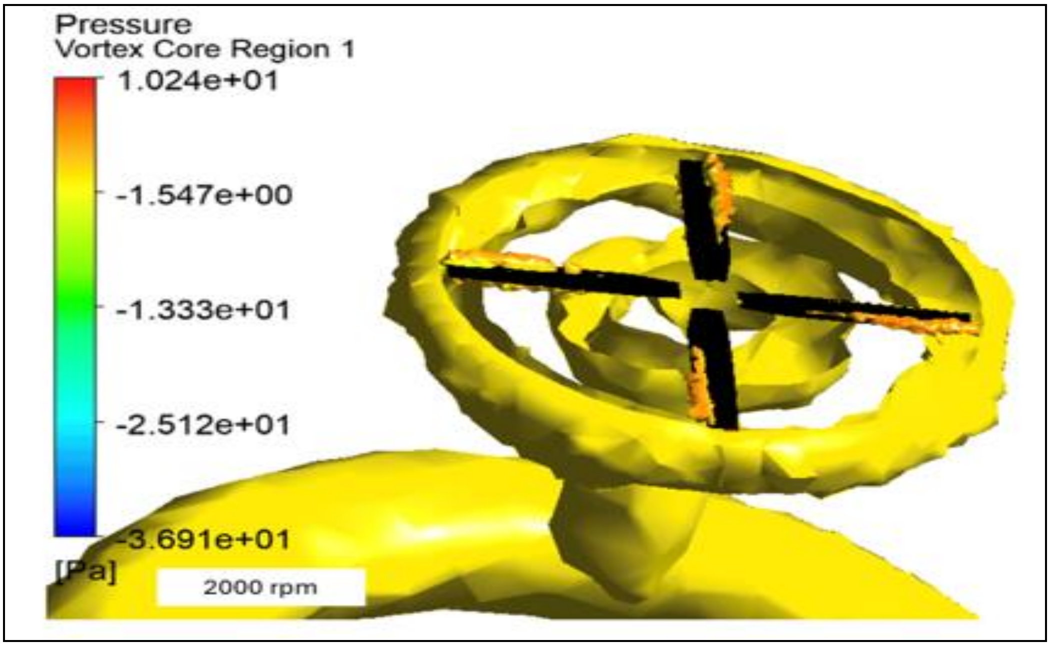

Fig 31: Q-criterion coloured for pressure – 2000 rpm case

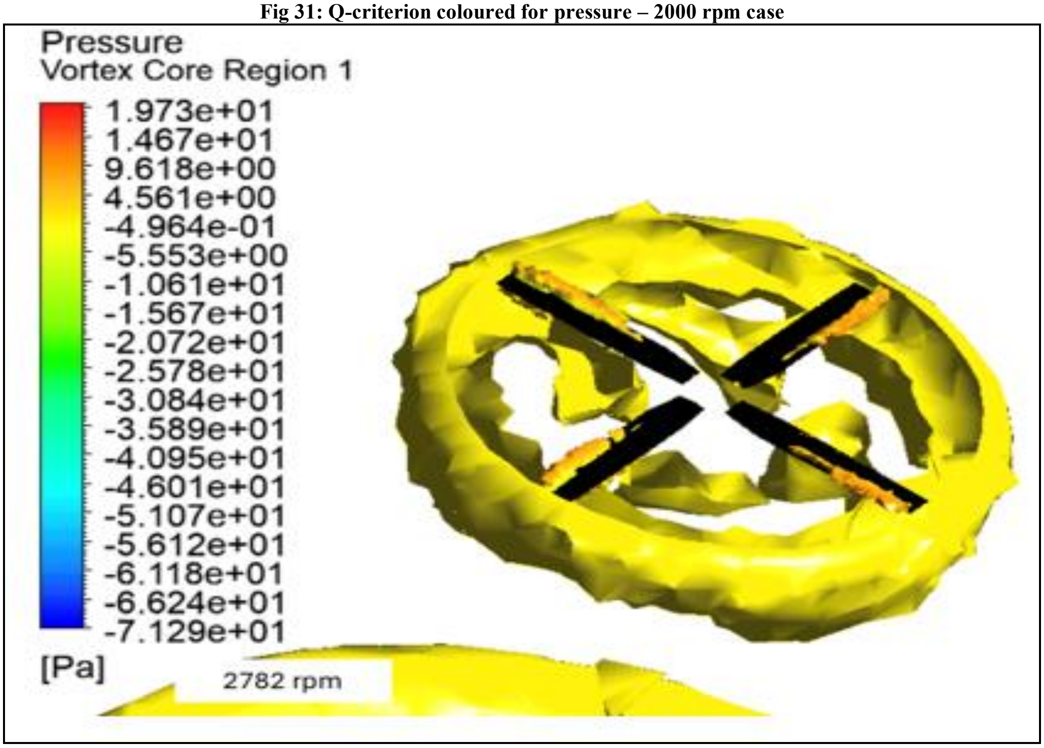

Fig 32: Q-criterion coloured for pressure – 2782 rpm case

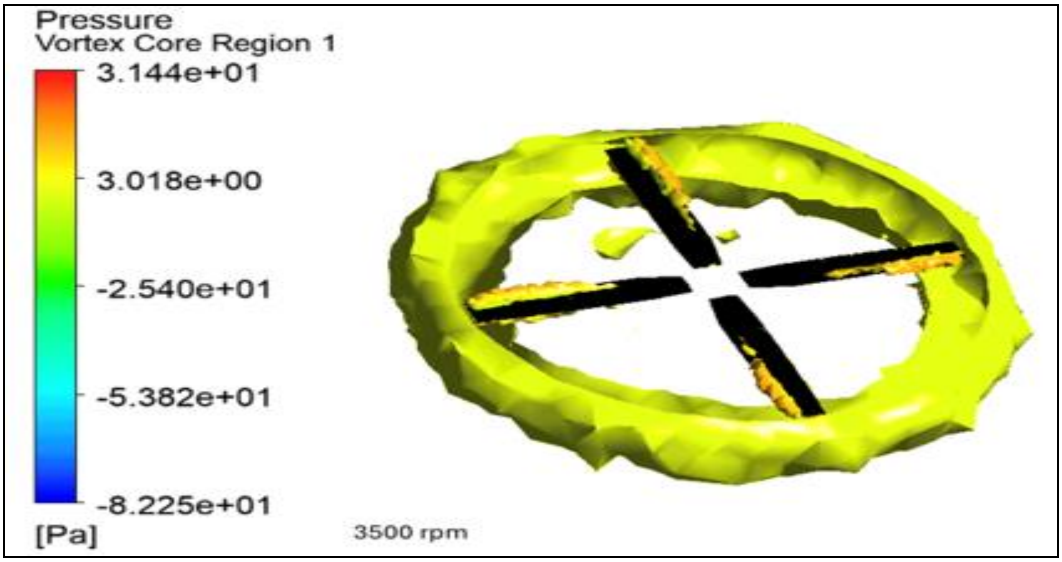

Fig 33: Q-criterion coloured for pressure – 3500 rpm case

From the Q-criterion plots, although low in detail, the tip vortices can be identified and the flow vorticity on the trailing edge of the outboard portion of the blade. The continuous ring indicates that the blades are continuously ingesting the blade tip vortices with each rotation.

Figs. 34-36 presents plot for the turbulent kinetic energy at an intersection plane through the centre of the rotating domain on the $zx - axis$. The TKE in front of the blade indicate the presence of BVI where the blade tip has the maximum TKE value.

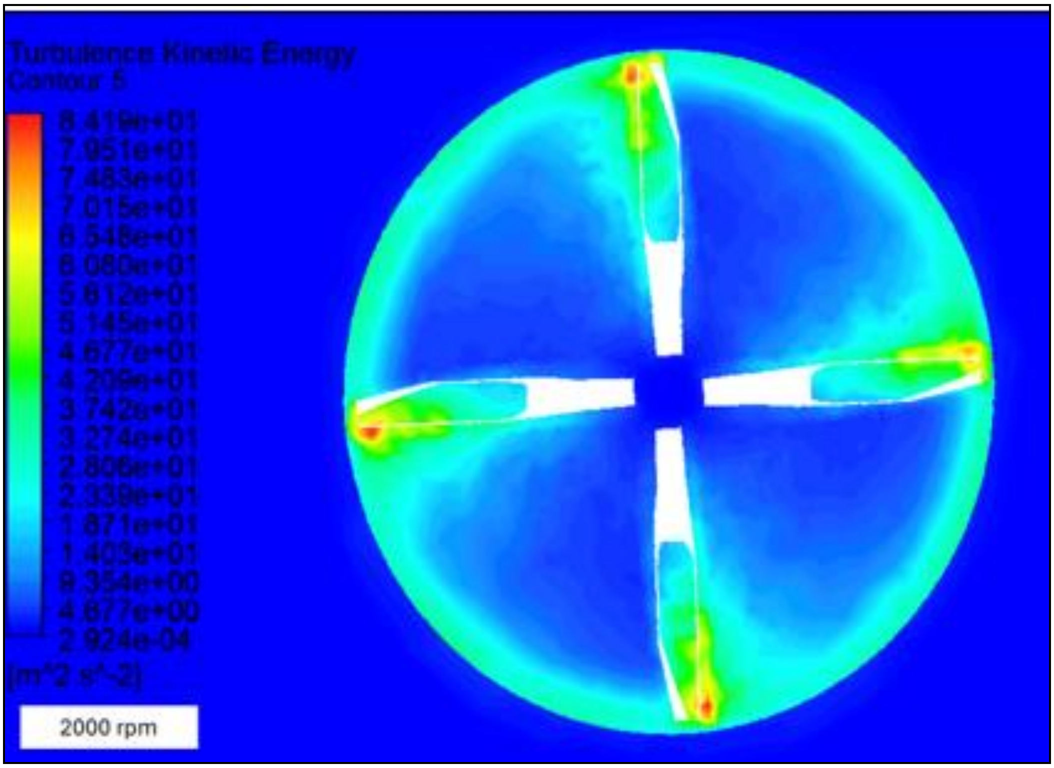

Fig 34: Turbulent Kinetic Energy (TKE) across the rotor disk – 2000 rpm case.

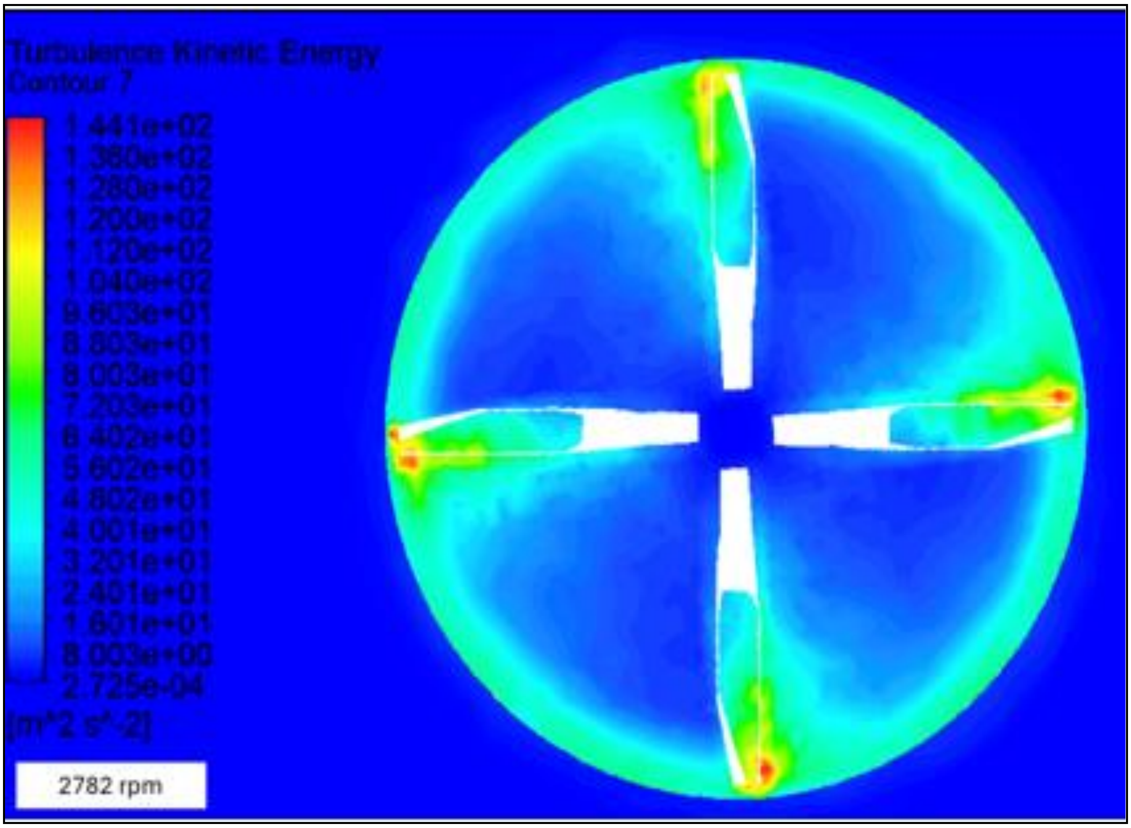

Fig 35: Turbulent Kinetic Energy (TKE) across the rotor disk – 2782 rpm case.

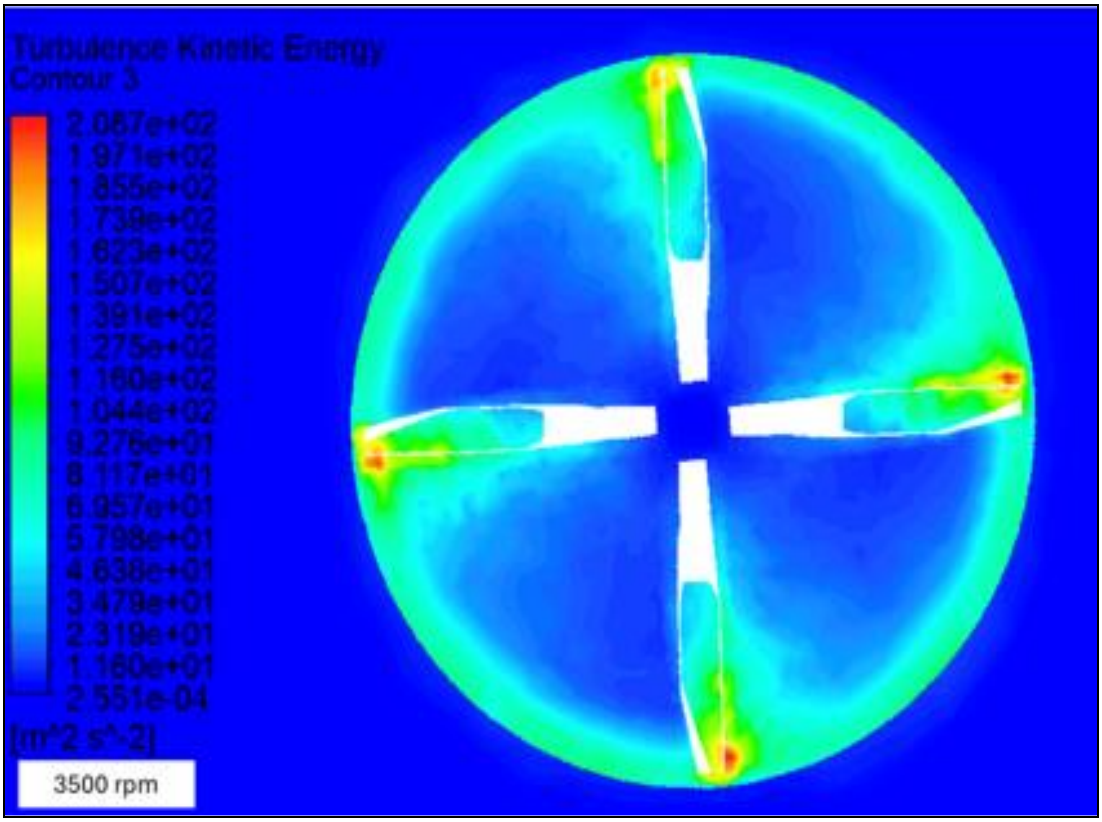

Fig 36: Turbulent Kinetic Energy (TKE) across the rotor disk – 3500 rpm case.

In conjunction with the use of inflation layers the calculation of suitable wall functions and y^+ values ensure further accuracy in the simulations. The y^+ value is a dimensionless parameter used to characterise the near wall mesh resolution in CFD simulations. It represents the distance from the wall to the first computational cell centre, normalised to the distance to the nearest wall (the walls boundary layer thickness). A low y^+ value indicates that the first computational cell is in the viscous sublayer where the flow is strongly influenced by viscosity and where the no-slip boundary conditions apply. A high y^+ value indicates that the first computational cell is located further away from the wall within the log-law layer where the flow is less influenced by viscosity and all wall functions can be applied. The inclusion of an appropriate y^+ value ensures that the mesh resolves the boundary layer at the rotor blade surface by placing the first computational cell within the boundary layer allowing for in depth analysis on the flow over the aerofoil profile.

7. Conclusions And Future Pathways

A detailed CFD investigation has been conducted to explore the current ongoing research into rotor blade optimisation for powered rotary-wing flight on Mars. Inspiration was taken from the recent Mars 2020 mission which included a small rotorcraft named Mars Ingenuity. The success of MARS ingenuity hexacopter initiated studies into improving future rotor performance with a conceptual design for a new rotor blade being published by those at NASA and JPL. The foundations for this rotor blade were adopted and implemented into Ansys Fluent to observe the flow characteristics at varying rotor speeds: 2000 rpm, 2782 rpm and 3500 rpm. The initial conceptual design by JPL gave an estimation of the optimum rotor speed at 2782 rpm and so this value formed the jumping off point for the values either side. A crucial factor in Martian flight is the requirement for the rotor to spin at speeds much faster than terrestrial helicopters on Earth and so a common testing metric is the thrust output; each rotor speed was simulated to find out which case produced the most thrust. These values were compared to a study conducted by NASA for a similarly low atmospheric pressure density. Results for thrust were output at 0.39 *N*, 1.07 *N* and 1.57 *N*, respectively showing that the requirement for higher rotor speeds is validated by the inadequate thrust performance of the 2000 rpm case. The flow behaviour for each case followed similar trends with differences in velocity and pressure values. The mesh density utilized was adequate to visualize quite accurately key rotary aerodynamic characteristics such as the blade tip vortices, surface pressure difference and streamlines were identified. Future investigations may explore gust loading and also fluid-structured interaction (FSI) as the blades are compliant, i.e. flexible. Other areas for future investigation include blade twist. The conceptual design by JPL gave a linear twist from root to tip off 18° for the optimised rotor blade. Future simulations should include this adjusted geometry and compare with results for thrust now that the output range is known. Efforts in these directions are currently underway utilizing ANSYS workbench and will be reported soon.

References

[1] O. Beg, S. Kuharat, A. Kadir, W. Jouri, CFD simulation of diamond and zinc smart nanoparticles performance in a water-based trapezium direct absorber solar collector, *Materials of the Future: Smart Applications in Science and Engineering 2021*.

[2] A. Imam, R. Bicker, Effects of propeller blade twist on reconnaissance quad-rotor UAV, in *Proceeding of,* Military Technical College, pp. 1-15.

[3] H. Shao, D. Li, Z. Kan, H. Li, D. Yuan, J. Xiang, Influence of wing camber on aerodynamic performance of flapping wing rotor, *Aerospace Science and Technology,* Vol. 113, pp. 106732, 2021.

[4] K. Pandey, U. Kumar, G. Kumar, D. Deka, D. Das, A. Surana, CFD analysis of an isolated main helicopter rotor for a hovering flight at varying RPM, in *Proceeding of,* American Society of Mechanical Engineers, pp. 543-551.

[5] K. Corfeld, R. Strawn, L. Long, Computational analysis of a prototype martian rotorcraft experiment, in *Proceeding of,* 2815.

[6] L. A. Young, E. Aiken, M. Derby, R. Demblewski, J. Navarrete, Experimental investigation and demonstration of rotary-wing technologies for flight in the atmosphere of mars, *58th Annual Forum of the AHS, International, Montreal, Canada, June 11-13, 2002.*, 2002.

[7] M. Ammoo, Z. Awal, Main Rotor Blade Air Flow Characteristics & Behaviour of a Remote Controlled Sub-scale Helicopter: A Case Study, *International Journal of Research in Aeronautical and Mechanical Engineering,* Vol. 1, No. 7, pp. 228-235, 2013.

[8] A. Fluent, Ansys Fluent Theory Guide, *ANSYS Inc*, 2011.

[9] B. T. Pipenberg, M. Keennon, J. Tyler, B. Hibbs, S. Langberg, J. Balaram, H. F. Grip, J. Pempejian, Design and fabrication of the mars helicopter rotor, airframe, and landing gear systems, in *Proceeding of,* 0620.

[10] G. J. Leishman, 2006, *Principles of helicopter aerodynamics with CD extra*, Cambridge university press,

[11] W. Johnson, S. Withrow-Maser, L. Young, C. Malpica, W. J. Koning, W. Kuang, M. Fehler, A. Tuano, A. Chan, A. Datta, *Mars science helicopter conceptual design*, pp. 2020.

[12] W. J. Koning, E. A. Romander, W. Johnson, Optimization of low Reynolds number airfoils for Martian rotor applications using an evolutionary algorithm, in *Proceeding of,* 0084.

[13] S. Kuharat, O. A. Bég, A. Kadir, T. A. Bég, W. Jouri, Computation of gold-water nanofluid natural convection in a three-dimensional tilted prismatic solar enclosure with aspect ratio and volume fraction effects, *Nanoscience and Technology: An International Journal,* Vol. 11, No. 2, 2020.

[14] M. J. Akbar, O. Anwar Bég, T. Anwar Bég, M. M. Bhatti, A. Kadir, S. Kuharat, CFD simulation of turbulent aerodynamics of a hummingbird wing for gliding micro-UAVs, *Journal of Computational Applied Mechanics,* Vol. 57, pp. 230-256, 2026.

[15] S. Kuharat, O. Anwar Bég, A. Kadir, B. Vasu, Computation of metallic nanofluid natural convection in a two-dimensional solar enclosure with radiative heat transfer, aspect ratio and volume fraction effects, *Arabian Journal for Science and Engineering,* Vol. 45, No. 11, pp. 9075-9093, 2020.

[16] S. Kuharat, M. Chaudhry, O. A. Beg, T. A. Bég, Computational hemodynamic simulation of non-Newtonian fluid-structure interaction in a curved stenotic artery, *European Mechanical Science,* Vol. 8, No. 4, pp. 226-256, 2024.

[17] S. F. Ramadan, M. M. Bhatti, K. S. Mekheimer, A. M. A. S. Moawad, C. M. Khalique, Magneto-Bioconvection Dynamics of Synovial Nanofluids: Consequences of Porosity, Rheology, and Heat Generation, *Journal of Computational Applied Mechanics,* Vol. 57, No. 1, pp. 122-133, 2026.

[18] H. A. Daud, Q. Li, O. A. Bég, S. AbdulGhani, Numerical investigations of wall-bounded turbulence, *Proceedings of the Institution of Mechanical Engineers, Part C: Journal of Mechanical Engineering Science,* Vol. 225, No. 5, pp. 1163-1174, 2011.

[19] O. A. Bég, H. Javaid, S. Kuharat, A. Kadir, H. J. Leonard, W. S. Jouri, T. A. Bég, V. Prasad, Z. Ozturk, U. F. Khan, *Computational fluid dynamic simulation of thermal convection in green fuel cells with finite volume and lattice Boltzmann methods*, in: *Energy Conversion and Green Energy Storage*, Eds., pp. 133-170: CRC Press, 2022.

[20] O. A. Bég, S. Kuharat, T. A. Bég, J. Pattison, A. Kadir, H. J. Leonard, W. Jouri, *Two-Way Fluid-Structure Interaction Hydroelastic Simulation of Vibrating Membranes with Applications in Marine Renewable Wave Power*, in: *Eco-Materials and Green Energy for a Sustainable Future*, Eds., pp. 295-329: CRC Press, 2024.

[21] M. E. GENDY, O. A. Bég, A. Kadir, M. Islam, D. Tripathi, Computational fluid dynamics simulation and visualization of Newtonian and non-Newtonian transport in a peristaltic micro-pump, *Journal of Mechanics in Medicine and Biology,* Vol. 21, No. 08, pp. 2150058, 2021.

[22] B. N. Perez Perez, *Rotor CFD Analysis at Terrestrial and Martian Atmospheric Densities*, pp. 2018.